THE EFFECTIVENSS OF BIOMIMETIC SINUSOIDAL LEADING EDGE IN IIMPROVING STABILITY PERFORMANCE OF CONTROL-LINE AIR MODLE PLANE

by

Letong Xu

International Department

Beijing National Day School

August 2020

Instructor

Bozhao Fan

Beijing National Day School

Tianxiang Hu

Beijing University of Aeronautics and Astronautics

THE EFFECTIVENSS OF BIOMIMETIC SINUSOIDAL LEADING EDGE IN IIMPROVING STABILITY PERFORMANCE OF CONTROL-LINE AIR MODLE PLANE

by

Letong Xu

Abstract

Leveraging theoretical analysis and experimental field flights, this paper investigated the root cause of the long haunting instability problem that found in F2B aero model plane's precision flight. Specifically, F2B model plane sometimes lost control unexpectedly in performing inside and outside loop maneuvers. This problem has existed for many years without a clear identification of root cause and without any effective remediation solution. In this research, the Kepner&Tregoe® Analytical Troubleshooting thinking processes were used to define the problem and find possible causes; high school Physics and extended knowledge of Aerodynamic theories have been applied to analyze and identify the true cause. A remediation solution is then introduced by leveraging flow control and biomimetic technologies. Inspired by humpback whale's unique flipper structure and tubercles on its leading edge, in this research, this special structure was modeled into a definitive sinusoidal leading edge for the model plane. It was simulated with CFD (Computational Fluid Dynamics) software, i.e. Fluent, to prove its effectiveness in increasing critical angle of attack and delay stall. The standard NACA0021 airfoil is employed in the study. This airfoil is commonly used in the control-line model plane. Two sets of sinusoidal leading edge were fabricated and installed on the plane for experiments. The actual effectiveness and differences between normal leading edge and sinusoidal leading edge were then tested and verified in the real flights using a 9-axis in-flight data recorder and video camera.

Content

1. Introduction

1.1 Introduction to Control-line Air Model Plane

Aeromodelling is a fascinating sport and hobby that attracts people from all ages. It is both fun and full of knowledge. With the fast development of science and technology, aeromodelling also evolved, however, the basic theories behind these small aircrafts are rather unchanged in the past decades.

The Federation Aeronautics International, FAI, which is the worldwide governing body of aeromodelling as a sport, has classified aeromodelling into three main categories based on the different ways of control. Those three are:

1) Free flight model aircraft, or F1 model, is the model plane that does not require control from the ground once takes off; it is indeed "free flight" in the air.

2) Control-line model aircraft, or F2 model, refers to the model plane that can be controlled by the pilot on the ground with a pair of tin lines that attached to the model's elevator; the other end of the two lines connect to a control handle that is operated by the pilot. The model is confined by the two control wires and can only make circular flights on the half hemisphere surface. The controlled elevator can make the plane to move up and down, or in the pitch axis. The combination of up-and-downs allows the model to make different shape of maneuvers, e.g. loops, squares, figure "8", etc. in that half hemisphere surface. See below illustration Fig. 1.1.

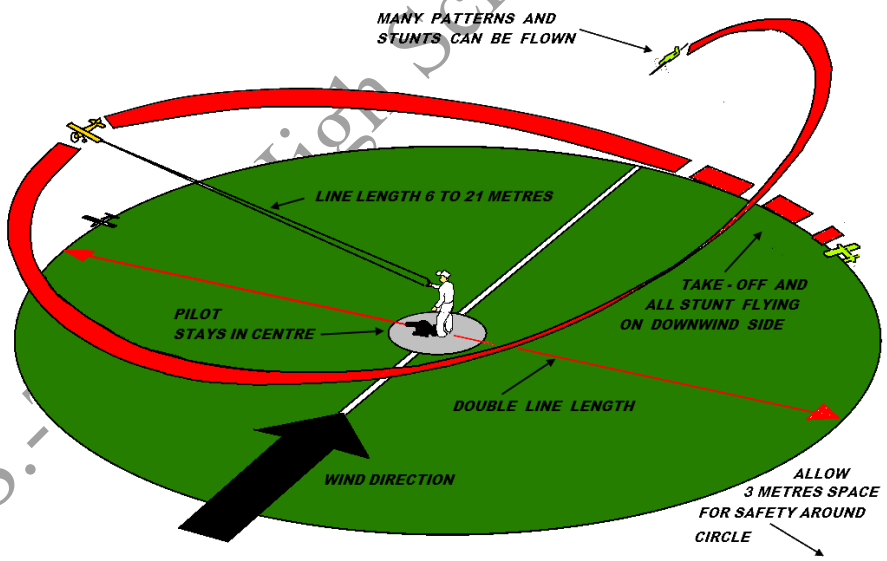

Fig. 1.1 diagram from http://www.control-line.org.au/whatis.htm

3) Radio-control model aircraft, or F3 model, which is controlled by the pilot from the ground by sending radio frequency control signals that are received by the receiver installed in the model plane and executed by a set of servos which connect to the different control surfaces, e.g. rudder, elevator, flaps, etc.

Within the category of F2 Control-line air model plane. There are 4 sub-categories, which are: F2A-CL Speed; F2B-CL Aerobatic; F2C-CL Team racing; F2D-CL Combat.

This paper and research focus mainly on the issue found in F2B Aerobatic.

F2B Aerobatic, or control-line stunt flight, is for the pilot to control the model plane to fly a preset schedule of maneuvers. It includes, for example, inside and outside loops, squares, triangle, four leaves clover, etc. In a competition, these maneuvers are scored by a panel of judges based on its accuracy and precision. The length of the control line for F2B is usually 18-20 meters long. The plane flies about 5.3 $^{+/-0.4}$ second per lap thus at an average level flying speed of 90-100km/h. The most common airfoil that used is the standard NACA0021 symmetric airfoil. The traditional F2B model is usually powered by 2-stroke or 4-stoke internal combustion engines. In the past 10 years or so, electric engine is more and more adopted in F2B as it is easy-to-use and is environmentally friendly.

Typical F2B models have wingspan of 1.4-1.5 meters, total wing area between 0.3-0.4 square meters, and a total take-off weight of 1.5-2.0 kilograms. See Fig 1.2.

Fig. 1.2 - Control line air model plane that I flew in the 2016 World Championship (To note, the thin yellow stripes and tapes are not part the original model. Those are temporarily fixed onto the wing in order to observe the air flow during flight, and to visualize possible stalls during maneuver.)

1.2 Problem definition

1.2.1 Discovery of the problem

Control line precision acrobatic flight is an official sport defined by FAI. I started to practice this sport since the age of nine and now am already into the 7th year of practicing. As stated in the early section of introductions, control line acrobatic flight

is for the pilot to control the model to make a preset sequence of 16 standard maneuvers, which includes level flight, inverted level flight, inside loop, outside loop, vertical “8”, four-leaf-clover, etc. In the standard competitions, a panel of judge scores each of the maneuvers the pilot has controlled the model to perform based on the maneuver’s complexity and accuracy. Therefore, it has a high demand of control precision from the pilot, and equally critical is a well-designed model aircraft. The first part is usually achieved by intensive trainings over time, and the later part requires the pilot to have knowledge in aerodynamics and a well-designed well-built air model plane.

Fig 1.3 - (a) is me operating my plane, (b) is when I represented the Team of China to participate in the World Championships in France, and (c) is when I won the title of World Champion.

Fig 1.4 - 2018 F2 World Championship (France) Award Ceremony

Over the past 6+ years, I have made more than 2000 training flights and had made great progress piloting the model to perform precise maneuvers. I won twice World Champion titles in France and Australia in F2 World Championship competitions and won a number of National Champion titles in China. However, for a long time, one issue continue puzzles me: that is, my plane sometimes become instable with sudden "shakes" when it is making high dynamic maneuvers, especially in condition of calm weather when the surrounding air is still or breezeless. This problem is especially obvious when I control the plane to perform 2-3 consecutive inside or outside loops. Interestingly, this kind of instability problem seldom happens in the first loop, and seldom in windy conditions. The occurrence of this problem is very detrimental; once it happens the model will likely go into an uncontrollable state and prone to crash. I have had a hard lesson in the 2016 F2 World Championship in Australia, when one of my primary models crashed because of such problem, just 2 days before the official competition.

In order to confirm if this is a common problem, I reached out to many professional operators and coaches including four senior world champions and a lot of experts in China and abroad, they all confirmed that this problem has long existed. From 1960s till now, many F2B pilots have been trying to solve this problem by changing the design, changing aerodynamic configuration, etc. but the outcomes are not satisfactory. A couple known experiments includes adding "turbulator" nodes or lines on the surface of the wing, however it all hasn't had much effect in reducing the instability issue of the plane. The USA F2 team once tried to use vortex generators on the wing but there were not sufficient evidence showing the vortex generator was making a difference for the F2B model planes, although it has proved to be effective on the full-size fixed-wing aircraft [1].

Fig 1.5 - Vortex Generator on Bone 737 [1]

In my early years of flying, I was insufficient

with my knowledge to do science research; it was neither a pressing issue because I had learnt an alternative work-around to overcome this problem, that is to make a step back when making the 2nd and the 3rd loop, then the "shake" problem would less likely to happen. However, along with the years of practicing the demand for operation accuracy and stability gradually intensified, the turbulence of the plane becomes the most influencing aspect which affected my performance in competition. To take another step in my journey to the top, the need to find a solution to this problem comes to the table. Meanwhile with accumulation of knowledge and grow in age, it is becoming more realistic for me to do an independent scientific research to fundamentally find the root case and solve the problem. All these above have led me to this paper of research.

1.2.2 Inside and outside loops

The model plane's instability problem is mostly seen in the loop maneuvers, hence it is necessary to first understand what a loop maneuver is.

Fig. 1.6 shows the actual flight when the pilot is performing the loop maneuvers. The dot line circle is manually added onto the original picture to illustrate the model plane's flying path of the loop.

Fig 1.6 - Loop maneuver

Per FAI F2B sports code [2][3], inside loop is specified in the following fig. 1.7. The pilot shall control the model to perform 3 consecutive, clock-wise, vertical loops with exactly the same size and position. The bottom of the loops shall be kept at 1.5 meter above the ground, and the top of the circle shall be at 45 degrees from the perspective of the pilot.

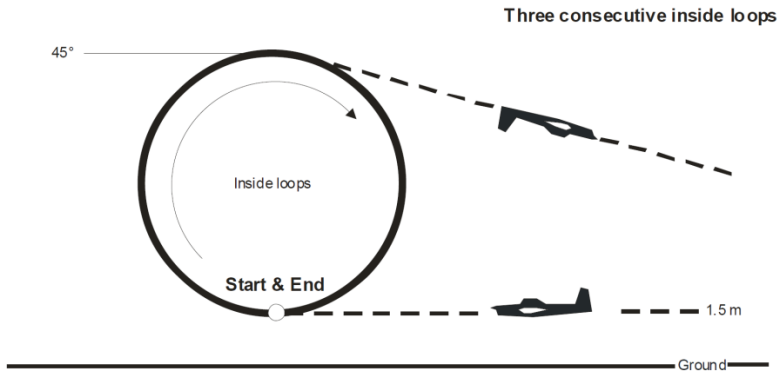

Fig. 1.7 - Inside Loop

The definition of outside loop is similar. The difference of outside loop is that it is entered from inverted flight, and the loop is flown counter-clock-wise.

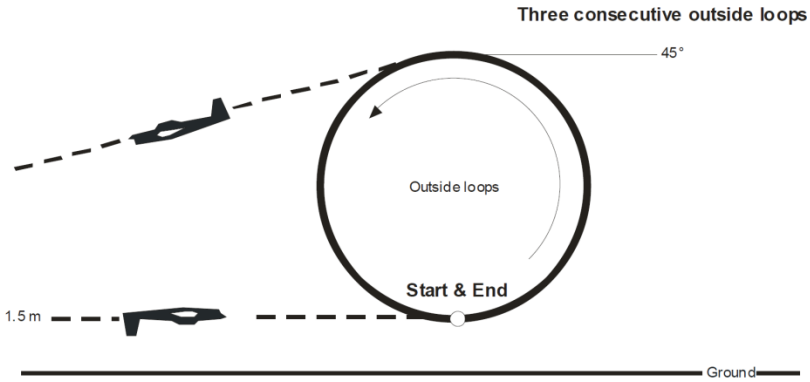

Fig. 1.8 - Outside loop

1.3 Problem analysis

1.3.1 Initial Analysis of Possible Causes

Kepner & Tregoe Analytical Troubleshooting (ATS) [4] is a methodology as well as a thinking process to systematically identify and define problems, find possible causes and true cause, define solutions to solve the problem, and think beyond the fix. This thinking process is applied in this research.

The first step of the process is to clearly define the problem with details. This is a vital step as all the later research will have to rely on accurate understanding of the problem in the first place. A specific technique of ATS is to categorize the problem in a way of “IS” and “IS NOT”. This approach helps to trigger the thinking of probable causes by verifying each pair of “IS” and “IS-NOT” and finding differences between the two.

Applying the Kepner & Tregoe Analytical Troubleshooting thinking process, the definition and details of the problem is specified as below:

Problem Definition: Control line model plane becomes occasionally instable in performing 2nd and 3rd consecutive loop maneuvers.

	The problem IS observed in …	**The problem IS NOT observed in …**
What	F2B regular size model plane	Small size control line models In-door control line models Radio control models/free flight models
Where	Outdoor More prone in side-wind or opposite-wind locations Loop maneuver Lower part of the loop	In door (Regula F2B does not fly in-doors) down-wind locations Other maneuvers (horizontal "8", square "8" etc. Upper part of the loop
When	No wind or light wind conditions (wind speed less than 1-2meter/second) 2nd and 3rd consecutive loop	Windy conditions 1st loop if only one loop is performed if I make a step back when performing the 2nd and 3 loops
Extent of the problem	Controllability reduced. Severity varies from time to time.	Increasing controllability Predicable or constant There is no pattern that 2nd loop is better or worse than the 3rd loop.

Table 1.1

The fact that the instability issue only happens in the 2nd and 3rd loop but not in the first one suggested that the condition of the model or the external environment might have changed between the first loop and the consecutive ones. This could be the changes in the model's speed or changes in the environmental airflow in that flying space.

The fact that the instability issue normally happens in lower part of the inside loop but not at the upper part of the circle has suggested that this MAY be related to the speed change of the model during the loop.

The fact that the instability issue normally happens with the regular F2B model but not with the smaller size control-line models or in-door control-line models suggested me to further investigate the key differences among the three. It is obvious that the latter two kinds of control-line models are much smaller in size, much lighter in weight, much thin with its airfoils, and with much smaller propellers. What all these lead to is an assumption that they are not powerful enough to change the environmental air condition along the flying path, compared with the full-size model. Or in other words, the possible cause is that the full-size control-line model might have generated turbulent air flow along the flying path that caused the consecutive loops to have been impacted by these currents. This can well explain why the problem is more prone to happen when there is no wind, as the wind can help to "blow away" the turbulent airs that the model has left behind. Similarly, this can also explain why it could overcome the problem if the pilot makes a step back from the center of the flying circle, as this move changes the physical position of the aircraft to "escape" from the turbulent zone that generated by the plane in previous loops.

Summarizing the above, there are two hypothetical causes that can be established which might have triggered the model to become instable in loops.

1. The model creates turbulent air flows along the flying path when performing the 1st loop. These unstable current leaves an impact to the model on the consequent loop maneuvers in close proximity to the same path, the model is then flying in a large angle of attack and caused the airflow to separate from the wing surface. The lift on the wing sharply drops and the force acts on the wing becomes imbalanced. To that moment, the turbulent condition is established and observed.

2. The decrease of flying speed in the loop, especially during vertical climbs, makes the stall worse, which further reduced the wing's lift force and causes the model to be unstable or uncontrollable.

1.3.2 Verify the true cause

The two possible causes above can provide logical explanations to most of the symptoms that have been listed in the problem specifications in 1.3.1. However, these hypothesizes will have to be proved in theory to be precise and accurate, and to be verified in actual flights as well.

The following sections focus on the theoretical tests to these possible causes, using physics from high school, and using my extended study in aerodynamic theories.

2. Theoretical Analysis

2.1 Introduction

In order to validate the true cause of the control line model instability issue in loop maneuvers, and provide a theoretical explanation against the true cause, in this chapter, analysis have been made by applying high school physics knowledge coupled with extended aerodynamic theories.

2.2 Control line maneuvers and analysis

2.2.1 Level flight analysis

Level flight is the most basic movement in control line model plane flying. It refers to the model's horizontal circular flying parallel to the ground at the height of 1.5 meters in constant speed. Two laps of level flight are required before any maneuver that the pilot will perform. Therefore, it is essential to understand how it works.

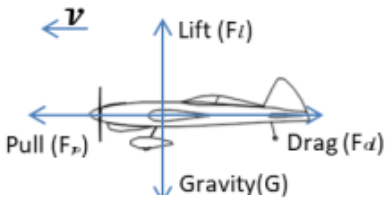

Fig. 2.1

Assume the lap time (t) is 5.3 seconds. This is measured in actual flight. The radius (r) of the circle is 21.5 meters. The speed of the model (V) can be calculated as the following, where D is the model's flying distance per lap.

$$V = \frac{D}{t} \quad (1)$$

$$D = 2\pi r \quad (2)$$

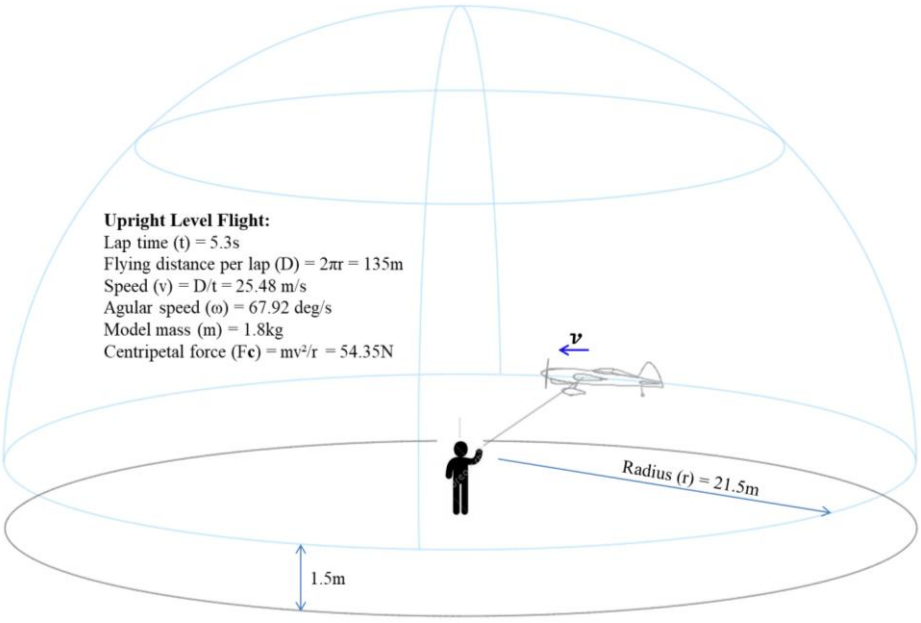

Fig. 2.2 - Upright level flight

In the force analysis that illustrated in fig. 2.1, there are 5 forces exerted on the plane, those are: Gravity (*G*), Lift force (F_l) generated by the wing, Pull force (F_p) from the engine/propeller and Drag force (F_d) from the air. The fifth is the Centripetal force (*Fc*) given by the pilot via the control lines. This last force is perpendicular to the rest of the four forces and can be calculated with the following:

$$Fc = \frac{mv^2}{r} \tag{3}$$

In the above formula, *m* is the mass of the model, *v* is the flying speed, and *r* is the radius of the circle.

When the model is flying in constant speed, by Newton's first law of motion, the Pull force (F_p) equals to the magnitude of Drag force (F_d); similarly, as the model does not have vertical movement in level flight, the Lift force (F_l) equals to Gravity (*G*).

However, in order for the plane to obtain the sufficient lift force, the wing will have to fly with a certain Angle of Attack (AoA, or α), the forces exerted on the wing will become a little more complicated as illustrated in Fig. 2.3 below:

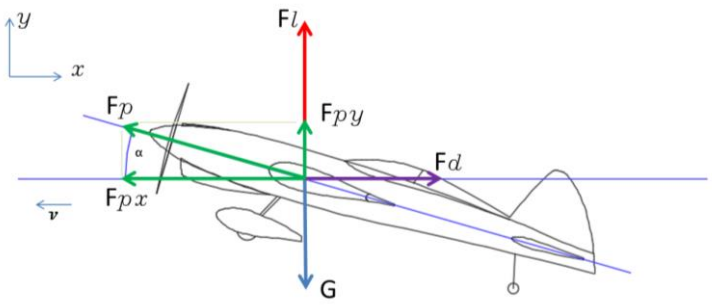

Fig. 2.3

As the engine and propeller installation is fixed on the airplane, the pull force that is generated by the propeller/engine is always parallel to the center line of the fuselage, and therefore, when the plane is tilt in the α angle of attack, the pull force *Fp* will then have two decomposition forces at the x-axis (*Fpx*) and y-axis (*Fpy*).

$$F_{px} = F_p \times cos\ \alpha \tag{4}$$

$$F_{py} = F_p \times sin\ \alpha \tag{5}$$

In level flying, the speed of the model is constant and there is no vertical movement at the y axis. By Newton's first law of motion, the resultant forces at the two directions, expresses as *Fx* and *Fy* must be zero:

$$Fx = F_{px} - Fd = F_p cos\ \alpha - Fd = 0 \tag{6}$$

And

$$Fy = (F_l + F_{py}) - G = F_l + F_p sin\ \alpha - G = 0 \tag{7}$$

As observed the in the actual level flight, the wing has a very small angle of attack (α), usually not more than 1 degree. Thus sin(α) ≈ 0 and cos(α) ≈ 1. In such condition, it is approximated that:

$$Fx = F_p - F_d = 0, or, F_p = F_d; \quad (8)$$

$$Fy = F_l - G = 0, or, F_l = G. \quad (9)$$

These basic assumptions and analysis are used in the next section of analysis.

2.2.2 Inside-loop analysis

The main purpose of this research is to find out the cause of the turbulence when the model is performing inside and outside loops; therefore, it is essential to understand the mechanisms behind these two maneuvers. As the inside loop and outside loop are very much of the same in shape and are only different in the flying direction, the theories of the two maneuvers are the same. Therefore, this section only focuses on the inside loop.

As earlier explained in 1.2.2, the inside loop maneuver is for the model to perform 3 consecutive, clock-wise, vertical loops with exactly the same size and position. The bottom of the loops shall be kept at 1.5 meter above the ground, and the top of the loop shall be at 45 degrees from the perspective of the pilot.

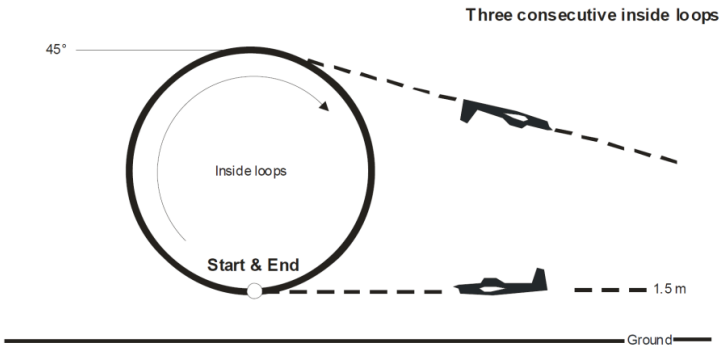

Fig. 2.3

Once the model starts the loop maneuver from level flying, an angle will be formed between the vertical direction from the ground and the yaw direction of the model plane. This angle is expressed as θ in the following illustration Fig. 2.4. For simplicity, assume the airplane flies with a very small Angle of Attack (AoA, α) during the loop, with such assumption, only the *G* force changes at the x and y direction at the different positions of the loop. Note the x, y coordinate system is rotated clockwise at the angle of θ for easy illustration in Fig. 2.4.

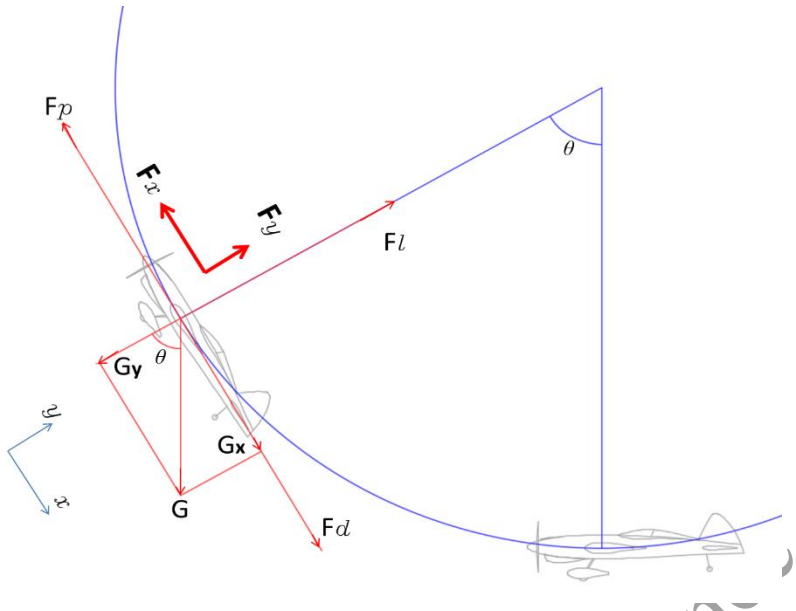

Fig. 2.4

The *G* force has two component forces at the x and y direction, respectively marked as *Gx* and *Gy*. That $Gx = G \times sin\,\theta$ and $Gy = G \times cos\,\theta$

In the x direction, the resultant force, *Fx*, is:

$$Fx = Fp - (Fd + Gx) = Fp - (Fd + G \times sin\,\theta) \quad (10)$$

In the y direction, the resultant force, *Fy*, is:

$$Fy = Fl - Gy = Fl - G \times cos\,\theta \quad (11)$$

The force in the x direction (*Fx*) changes the speed of the plane and the force in the y direction provides the centripetal force *Fc* that needed for the circular movement. That is to say, we can consider *Fy* and *Fc* is the same.

As illustrated in Fig. 2.5. At point A, $\theta = 0°$, $\sin\theta = 0$ and $\cos\theta = 1$, the forces exerted on the plane is similar as it is making level flight only the lift force F*l* become larger to give a centripetal force for the plane to perform circular motion. At this moment *Fc* = *Fl* -*G*

At point B, $\theta = 90°$, $\sin\theta = 1$ and $\cos\theta = 0$, the plane is moving straight upward. The direction of drag force *Fd* and the pull force *Fp* become vertical. The centripetal force was given solely by the lift force *Fl* of the plane. That is *Fc* = *Fl*

At point C, which is the top of the loop, the plane flies up-side-down. $\theta = 180°$, $\sin\theta = 0$ and $\cos\theta = -1$, The lift force *Fl* from the wing points downwards to the ground. The resultant force of lift *Fl* and weight *G* form the centripetal force. *Fc* = F*l* +*G*.

Point D is opposite to point B, $\theta = 270°$, $\sin\theta = -1$ and $\cos\theta = 0$, The plane is heading straight downward. The centripetal force is provided by the lift force. I.e. *Fc* = F*l*

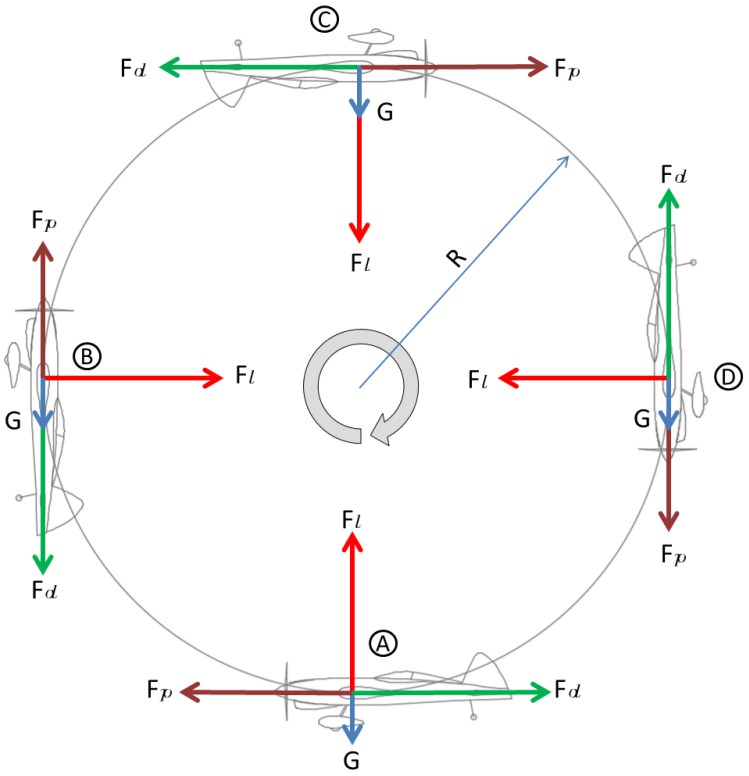

Fig. 2.5

Per F2B standard definition of inside loop maneuver, the radius (R) of the loop can be calculated as below:

$$R = r \times sin\left(\frac{45^\circ}{2}\right) = 21.5 \times sin\,22.5^\circ = 8.23m \quad (12)$$

The centripetal force that needed for the plane to perform such a loop can be calculated using formula (3)

In the previous level flight analysis in 2.2.1, it is concluded that the lift force in level flight approximately equals to the weight of the plane. A standard model plane weights about 18N, and therefore the lift force generated by the wing is about 18N during level flight.

In the inside loop maneuver, however, the centripetal force (Fc) is:

$$Fc = \frac{mv^2}{R} = \approx 142N \quad (13)$$

This centripetal force is primarily provided by the wing; therefore, it is obvious that it requires the wing to generate much more lift force in loops than in level flight. The only way to produce such strong force is to increase the angle of attack (AoA). In such situation, this AoA can no longer be omitted. It must be considered in the force analysis for loop maneuvers.

The below diagram Fig. 2.6 illustrated the force analysis when AoA (α) is considered.

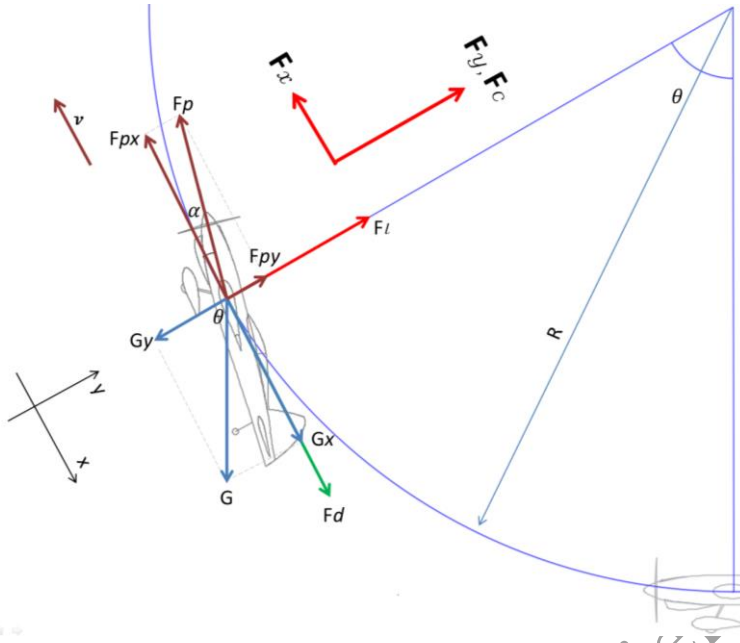

Fig. 2.6 - force analysis in large AoA

In the above Fig. 2.6:

1. The x, y coordinate system is rotated clockwise at the angle of θ for easy illustration.
2. The angle of attack (α) is the angle between the center line of the fuselage and the tangent line of the loop.
3. Model plane's movement direction parallels to x-axis, or tangent to the loop.
4. Lift force is represented as *Fl*.
5. The gravity of the plane is *G*, the two component forces at x, y directions are *Gx* and *Gy*.
6. The pull force from the propeller is *Fp*, because of the relatively large AoA, the direction of *Fp* can no longer be approximated to the same movement direction, and thus *Fp* has two component forces at x, y axis. They are expressed in the diagram as *Fpx* and *Fpy*.
7. The drag force is showed as *Fd*. The direction of *Fd* is opposite to the moment direction.
8. The total resultant force at y direction is represented as *Fy*, it is equivalent to centripetal force *Fc*.
9. The total resultant force at the movement direction, or x direction, is *Fx*.

The outcome of the component force analysis is the following:

$$Fx = Fpx - (Fd + Gx) = Fp\,cos(\alpha) - Fd - G\,sin(\theta) \quad (14)$$

$$Fy = Fl + Fpy - Gy = Fl + Fp\,sin(\alpha) - G\,cos(\theta) \quad (15)$$

$$Fc = Fy \tag{16}$$

Combine equation (15), (16) and (13):

$$Fc = \frac{mv^2}{R} = Fl + Fp \sin(\alpha) - G\cos(\theta) \tag{17}$$

2.2.3 Understand plane's speed and Angle of Attack in loop maneuver

When the model plane enters into the first loop from level flying, refer to fig. 2.5, at point A, the plane does not have instant change in speed. The plane maintains at 25.48m/s with very small AoA, thus $\alpha \approx 0$, and $\theta \approx 0$, therefore, $\sin(\alpha) = 0$, $\cos(\alpha) = 1$, and $\cos(\theta) = 1$, the equation (17) is then simplified as:

$$Fc = Fl - G \tag{18}$$

Therefore, the required lift force is:

$$Fl = \frac{mv^2}{R} + G \tag{19}$$

According to aerodynamic lift-line theory, the lift force that generated by the wing can be calculated with the following equation:

$$Fl = Cl\ \frac{1}{2} v^2 s\rho \tag{20}$$

Where *Cl* is the coefficient of the airfoil, *v* is the speed of the aircraft, *s* is the wing area, and ρ is the density of the air.

Compare equation (19) and (20), we know:

$$Fl = \frac{mv^2}{R} + G = Cl\ \frac{1}{2} v^2 s\rho \tag{21}$$

Therefore, where air density at 25°C $\rho = 1.184 kg/m^3$, *v* = 25.48m/s, *s* = 0.3395m^2, *R*=8.23m, *m*=1.8kg, *g*=9.8m/s^2

$$Cl = \frac{2m}{Rs\rho} + \frac{2mg}{v^2 s\rho} \approx 1.223 \tag{22}$$

As stated in the introductions, most F2B control-line model uses the standard NACA0021 or NACA0018 airfoil. NACA0021 is used in this research as this is the one that used on my model plane.

The lift coefficient of standard airfoil NACA0021 can be generated using the CFD program Xfoil. It is an interactive program for the design and analysis of subsonic isolated airfoils.

The only input that needed by Xfoil to generate lift coefficient is the Reynold number, or Re. This Reynold number can be calculated with the following equation:

$$Re = \frac{\rho v d}{\mu} \tag{23}$$

In the equation: ρ is the density of the air, v is the velocity of the plane, d is the average chord length of the wing and μ is the viscosity of the air.

Air density and the model's speed at the beginning point of the loop are known, that $\rho = 1.184 kg/m^3$, v = 25.48m/s. The average cord length of my model is 242.5mm. Air viscosity can be looked up from the website: https://www.engineeringtoolbox.com/, at 25 °C and 1 atmosphere pressure, $\mu = 18.37 \times 10^{-6}$

Therefore, Reynold number in this condition is: $Re \approx 4 \times 10^5$

The NACA0021 coefficient chart plotted by CFD Xfoil is showed in Fig. 2.8. The Angle of Attack for *Cl*=1.22 is approximately at 18 degrees. Note this angle is already close to the critical AoA of stall.

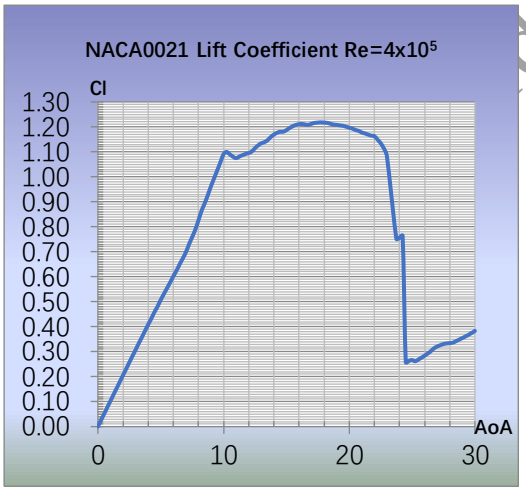

Fig. 2.8 - NACA0021 coefficient

Follow the same logic we will be able to know the AoA at any position of the loop, if we know the speed of the plane at that moment.

There are two ways that we can know the speed of the plane in loop: by calculation, or by measure the actual speed with a "speed meter", or Pitot tube, however the pitot is hard to be installed on the model plane.

To make it more intuitive, let's make an analogy. The movement of the plane in loop maneuver is similar to that of a roller coaster in the amusement park to perform loops; it is just that the centripetal force is provided by the wing for the plane, and by the push force from the track for the rollercoaster. The physics behind the two is the same.


Fig. 2.9 – Roller coaster loop

At the point when the roller coaster is entering a loop, it has already accumulated enough speed. The kinetic energy (E_0) at that speed (V_0) provides the momentum for the roller coaster to continue climbing up the loop. During this process, the initial kinetic energy (E_0) will become the sum of potential energy and kinetic energy at each particular moment. The total energy keeps unchanged in the process, if frictions are ignored. This can be expressed as:

$$E_0 = \frac{1}{2} m {V_0}^2 = \frac{1}{2} m {V_t}^2 + mg\delta h \quad (24)$$

Where V_0 is the initial speed at the bottom of the loop, V_t is the speed at any position when it climbs, δh is the elevated height, and m is the mass of the roller coaster.

On the first half of the loop, as the roller coaster climbs with increasing height, its potential energy increases, and the kinetic energy drops. Thus, the speed of the roller coaster decreases. When it reaches to the top, it has the highest potential energy and lowest kinetic energy, or lowest speed. On the second half of the loop when it dives, its potential energy drops and the kinetic energy increases, this makes the roller coaster to accelerate in the 2nd half of the loop. Theoretically, the total energy is constant in any position of the loop and the rollercoaster resumes with the same speed V_0 when it finishes the loop and passes the same bottom position the 2nd time.

As such, if we know the initial speed of the coaster, we will be able to calculate the speed at any given position of the circle V_t.

$$V_t = \sqrt{{V_0}^2 - 2g\delta h} \qquad (25)$$

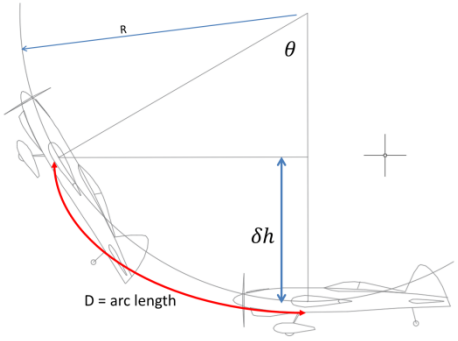

Fig. 2.10

This is almost the same as the model plane flying loops. However, the difference is that the plane's engine and propeller will generate the pull force (*Fp*). The work done by this pull force along the tangent path is added into the system. Meanwhile, when the model is flying with high speed, drag force from the air cannot be ignored; the result of this work by the drag force will reduce the plane's speed as it flies. The total resultant work from the engine and drag is the calculus of the resultant force in tangent direction (i.e. *Fx*) and traveled distance (i.e. length of the arc). This can be expressed as:

$$W_t = \int_0^\theta F_x D d\theta \qquad (26)$$

Where W_t is the total work that increased or decreased by the engine and by the drag force; F_x is the resultant force in the movement direction; and D is the distance the model has traveled from the bottom of the loop, this equals to the arc length that the model has flown.

Thus, the energy equation in (24) is adjusted as:

$$E_t + E_p = E_0 + W_t \qquad (27)$$

Or,

$$\frac{1}{2} m {V_t}^2 + mg\delta h = \frac{1}{2} m {V_0}^2 + \int_0^\theta F_x D \, d\theta \qquad (28)$$

Thus, the instant speed at any position, i. e. V_t , can be calculated with the following:

$$V_t = \sqrt{{V_0}^2 + \frac{2}{m}\int_0^\theta F_x D d\theta - 2g\delta h} \qquad (29)$$

In this equation, *Fx* is from equation (14), and

$$D = \frac{\pi R\theta}{180} \tag{30}$$

In the actual flight, the model plane is flying on the half hemisphere surface and the loop is not perpendicular to the ground, therefore, the actual height has a cos22.5° factor to the hypothetical vertical height of the loop, as illustrated in Fig. 2.11.

$$\delta h = R(1 - \cos\theta) * \cos(22.5°) \tag{31}$$

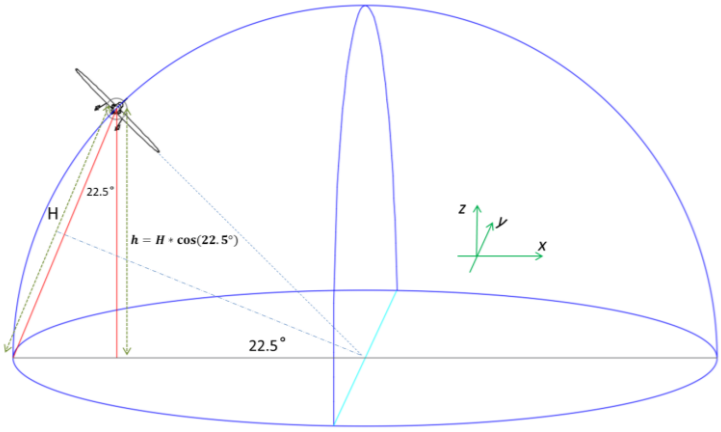

Fig. 2.11

Formula (29) has provided the theoretical way to calculate the speed of the plane in the loop maneuver. However, in this formula it is fairly difficult to do the calculus calculation of the work that yielded by the x-axis force. The full expression of this work is the following:

$$W_t = \int_0^\theta F_x D d\theta = \int_0^\theta (Fp\cos(\alpha) - Fd - G\sin(\theta))\frac{\pi R\theta}{180} d\theta \tag{32}$$

The difficulty to make this calculus can be overcome by using Microsoft Excel spread sheet to do an approximate simulation by dividing the entire loop into 720 small segments, i.e., to increase θ by 0.5 degrees per step from zero degree to 360 degree, these 720 steps form the entire loop. The following screenshot, Fig. 2.12, illustrated this calculation:

The drag force used in this simulation is from the following formula, where the drag coefficient is generated by Xfoil with Reynold number ranging from 2.2×10^5 to 4.0×10^5 to match the speed of the model plane.

$$F_d = \frac{1}{2} C_d * \rho s v^2 \tag{33}$$

The pull force is obtained by looking up the manufacturer's product specification of motor and propeller, Table 2. The motor used in this application is Sunny Sky 3120 brushless motor KV710 with Sail 12x6 inch 2-blade wood propeller. The power supply is from an 18.5V 5S 2950mah lithium polymer battery pack.

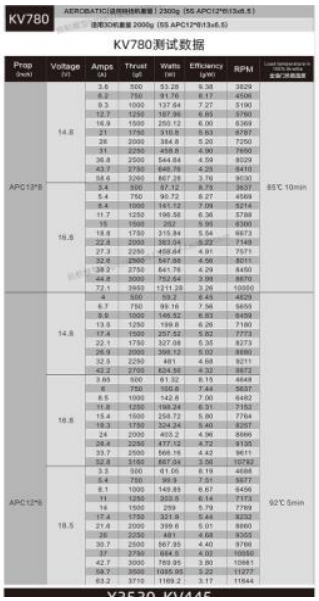

Table 2

Using this Microsoft Excel simulation, the speed changes are becoming visible. When the speed of each point is simulated, we can follow the same logic to calculate the needed lift force that has to be provided by the wing and from there the required lift coefficient (i.e. *Cl*) can be calculated. Once *Cl* is available, we can back-track the angle of attack AoA with CFD (Xfoil).

质量	1.8	ρ=	1.184
正筋斗半径	8.23	S=	0.3395
初速度V0	25.48		
迎角	18		

$$\frac{1}{2}mV_t^2 + mg\delta h = \frac{1}{2}mV_0^2 + \int_0^\theta F_x D$$

$$Fx = Fpx - (Fd + Gx) = Fp\cos(\alpha) - Fd - G\sin(\theta)$$

$$\Delta H = R(1-\cos(\theta)) * \cos(22.5) = 7.6035 * (1-\cos(\theta))$$

发动机拉力Fp	17
飞机阻力	10

θ	Fx	D	delta W	Wt	$E_0 = 1/2mV_0^2$	mg δ h		Vt=	ω	δ t	Time	ω	Vt
0.0	6.167961	0.07182	0.442985	0.442985	584.3074		649.7226	25.48966	177.4544	0.002818	0.002818	177.4544	25.48966
0.5	6.014025	0.07182	0.431929	0.874914	584.3074	0.005107	650.1969	25.48996	177.5192	0.002817	0.005634	177.5192	25.48996
1.0	5.8601	0.07182	0.420874	1.295788	584.3074	0.020428	650.6475	25.50779	177.5807	0.002816	0.00845	177.5807	25.50779
1.5	5.706199	0.07182	0.409821	1.705609	584.3074	0.045962	651.0745	25.51616	177.6389	0.002815	0.011265	177.6389	25.51616
2.0	5.552334	0.07182	0.39877	2.104379	584.3074	0.081706	651.4778	25.52406	177.6939	0.002814	0.014078	177.6939	25.52406
2.5	5.398515	0.07182	0.387723	2.492102	584.3074	0.127658	651.8576	25.5315	177.7457	0.002813	0.016891	177.7457	25.5315
3.0	5.244755	0.07182	0.37668	2.868782	584.3074	0.183815	652.2137	25.53847	177.7943	0.002812	0.019704	177.7943	25.53847
3.5	5.091065	0.07182	0.365642	3.234424	584.3074	0.250172	652.5462	25.54498	177.8396	0.002812	0.022515	177.8396	25.54498
4.0	4.937457	0.07182	0.35461	3.589033	584.3074	0.326724	652.8552	25.55103	177.8817	0.002811	0.025326	177.8817	25.55103
4.5	4.783942	0.07182	0.343584	3.932618	584.3074	0.413465	653.1406	25.55661	177.9206	0.00281	0.028136	177.9206	25.55661
5.0	4.630533	0.07182	0.332566	4.265184	584.3074	0.510389	653.4024	25.56174	177.9562	0.00281	0.030946	177.9562	25.56174
5.5	4.477242	0.07182	0.321557	4.586741	584.3074	0.617488	653.6407	25.5664	177.9887	0.002809	0.033755	177.9887	25.5664
6.0	4.324079	0.07182	0.310557	4.897297	584.3074	0.734755	653.8554	25.5706	178.0179	0.002809	0.036564	178.0179	25.5706
6.5	4.171056	0.07182	0.299566	5.196864	584.3074	0.86218	654.0467	25.57434	178.0439	0.002808	0.039372	178.0439	25.57434
7.0	4.018186	0.07182	0.288587	5.485451	584.3074	0.999753	654.2145	25.57762	178.0668	0.002808	0.04218	178.0668	25.57762
7.5	3.865479	0.07182	0.27762	5.763071	584.3074	1.147464	654.3589	25.58044	178.0864	0.002808	0.044988	178.0864	25.58044
8.0	3.712947	0.07182	0.266665	6.029736	584.3074	1.305302	654.4798	25.5828	178.1029	0.002807	0.047795	178.1029	25.5828
8.5	3.560603	0.07182	0.255724	6.285459	584.3074	1.473255	654.5773	25.58471	178.1161	0.002807	0.050602	178.1161	25.58471
9.0	3.408457	0.07182	0.244796	6.530256	584.3074	1.65131	654.6515	25.58616	178.1262	0.002807	0.053409	178.1262	25.58616
9.5	3.256521	0.07182	0.233884	6.76414	584.3074	1.839454	654.7023	25.58715	178.1331	0.002807	0.056216	178.1331	25.58715
10.0	3.104807	0.07182	0.222988	6.987128	584.3074	2.037671	654.7298	25.58769	178.1369	0.002807	0.059023	178.1369	25.58769
10.5	2.953326	0.07182	0.212109	7.199237	584.3074	2.245948	654.7341	25.58777	178.1375	0.002807	0.06183	178.1375	25.58777
11.0	2.80209	0.07182	0.201247	7.400484	584.3074	2.464268	654.7151	25.5874	178.1349	0.002807	0.064637	178.1349	25.5874
11.5	2.65111	0.07182	0.190404	7.590888	584.3074	2.692614	654.6729	25.58658	178.1291	0.002807	0.067444	178.1291	25.58658
12.0	2.500399	0.07182	0.179579	7.770467	584.3074	2.930969	654.6076	25.5853	178.1203	0.002807	0.070251	178.1203	25.5853
12.5	2.349966	0.07182	0.168775	7.939242	584.3074	3.179316	654.5192	25.58357	178.1082	0.002807	0.073058	178.1082	25.58357
13.0	2.199824	0.07182	0.157992	8.097234	584.3074	3.437634	654.4077	25.58139	178.0931	0.002808	0.075865	178.0931	25.58139
13.5	2.049985	0.07182	0.147231	8.244465	584.3074	3.705905	654.2732	25.57877	178.0748	0.002808	0.078673	178.0748	25.57877
14.0	1.900459	0.07182	0.136491	8.380956	584.3074	3.984108	654.1158	25.57569	178.0533	0.002808	0.081481	178.0533	25.57569
14.5	1.751258	0.07182	0.125776	8.506732	584.3074	4.272221	653.9354	25.57216	178.0288	0.002809	0.08429	178.0288	25.57216
15.0	1.602393	0.07182	0.115084	8.621816	584.3074	4.570224	653.7322	25.56819	178.0011	0.002809	0.087099	178.0011	25.56819
15.5	1.453876	0.07182	0.104418	8.726234	584.3074	4.878092	653.5061	25.56377	177.9703	0.002809	0.089908	177.9703	25.56377
16.0	1.305718	0.07182	0.093777	8.820011	584.3074	5.195804	653.2573	25.5589	177.9365	0.00281	0.092718	177.9365	25.5589
16.5	1.15793	0.07182	0.083163	8.903174	584.3074	5.523334	652.9858	25.55359	177.8995	0.002811	0.095529	177.8995	25.55359
17.0	1.010524	0.07182	0.072576	8.97675	584.3074	5.860657	652.6916	25.54783	177.8594	0.002811	0.09834	177.8594	25.54783
17.5	0.86351	0.07182	0.062018	9.037768	584.3074	6.207748	652.3749	25.54163	177.8162	0.002812	0.101152	177.8162	25.54163
18.0	0.716901	0.07182	0.051488	9.089256	584.3074	6.564581	652.0356	25.53499	177.77	0.002813	0.103965	177.77	25.53499

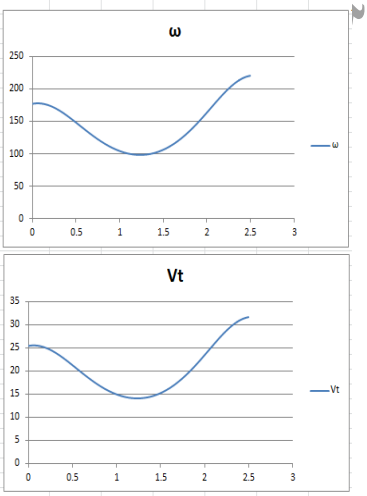

Fig. 2.12 – Speed simulation

The speed curve that generated from this simulation has a good match with the real flight data that recorded by the In-flight Data Recorder that installed on the model plane. A randomly chosen example is showed on chart to the right, Fig 2.13. The details of this flight data collection process are explained in section 4.1.

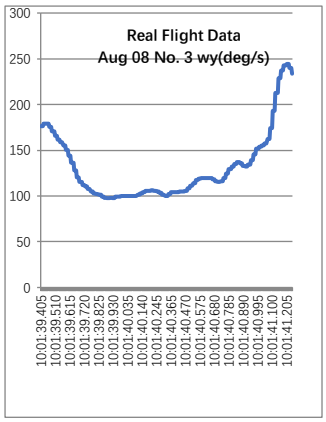

Fig. 2.13 – Actual speed in loop

2.2.4 Theoretical Conclusions

From the above analysis, in general, we see the largest lift force required in this maneuver is in the lower part of the loop, usually from 4-olock to 8-clock. With reverse calculations, we know the needed Angle of Attacks is beyond 14 degrees along this lower path. Refer to fig. 2.8, the lift coefficient from 14-degree AoA is starting to go flat and prone to enter into the stall zone. Any airflow turbulence may cause the AoA to change and in some occasions to increase, at which moment, the wing will stall and become unstable. This match well in the real situation when the plane completes the first loop, the air turbulence generated by this first maneuver may cause the model to stall when it performs the consecutive loops.

These above analyses provided a theoretical explanation of the root cause of the problem. To further match this with the real flight, a test model is prepared.

2.3 Prepare the Model Plane for Field Test

To be able to understand the airflow during the actual flight in a more intuitive manner, I made some modifications to my model plane. This is the plane that I have flown in the world championships and national championships. The design of this aircraft has many common attributes with most other F2B model planes and therefore it is a good representation. That means, if I can solve the problem on this plane, it is likely that the solution can apply to all other F2B model planes.

2.3.1 Initial Testing

The first experiment conducted was to observe the actual airflow over the wing during flight.

In order to do this, some 60 light silk threads were attached to the wing surface; each tread is about 7 centimeters long. The threads are fixed using adhesive tapes in 4 rows evenly distributed from the leading edge to the trailing edge. In each of the rows the spacing of thread is 10 centimeters. Yellow-colored threads are chosen as it provides the best visual contrast over the red background color and therefore is easily visible. A mini video recorder is mounted on the fuselage that can record movement of the threads during flight. The movement of the threads is a vivid illustration how the air flows over the surface of the wing. See below Fig. 2.14

Fig. 2.14

The actual testing flights were conducted twice on July 4th and 5th 2020 in Beijing "Element Football Park". Using these threads as indicators proved to be a very effective way to observe the airflow over the wing. The video footage clearly showed the airflow behavior during the entire flight. For example, the "panic" movement of the threads is a good indication of vortices or turbulence in a particular area on the wing. From the video, the "panic" movements of the threads are easily observed at the wing tips and during maneuvers, and especially it happened when the model plane become unstable. This is a factual proof that the instability of the model plane is caused by the separation of the airflow which causes stalls at some part of the wing

that makes the forces exerted on the wing imbalanced, at which moment, the "shake" would occur. The following video snapshot in Fig.2.15 shows the vortices at the wing tip. If we have a way to "control" the flow of the air, that will offer us an opportunity to avoid or delay the stall and hence improve the controllability of the plane during flight.

Fig. 2.15 Snapshot of flight video footage

2.4 Flow control

Flow control is a major rapidly evolving field of fluid dynamics. [5][6] It is one of the main ways to improve performance of planes. By using flow control techniques, it can serve large engineering benefit, like drag reduction, lift increase. In this research the main usage of flow control is to delay stall and increase the lift at high angle of attack.

Flow control can be divided into passive and active flow control, where passive flow control is to change the pre-setting of the plane before the flight to make improvement, and active control makes changes during the flight.

In passive flow control, a widely adopted method is to add vortex generator. The USA F2B National Team has once experimented using vortex generators on their competition model planes, however the general effectiveness of such measure was not very visible during flight and the same instability problem continue to exist.

There are a few ways to do active flow control, such as: Synthetic jet technique, Plasma flow control, intelligent material technology. However, these methods are generally too complicated to be applied on an air model plane with such a small size.

During my research on passive flow control, a past study caught my attention. It is to use bionic technique modeling the leading edge of the humpback whales and apply it to the leading edge of planes to help the aircraft to overcome stalls. It is found that humpback whales have many tubercles on their flippers, and these tubercles might have contributed to its agility during prey capture. Inspired by this, past researches proved that adding tubercles on the leading edge of the plane will help to increase the critical angle of attack of the wing and delay stalls to happen. This provides a great inspiration and opportunity to apply the same technique on air model planes. I

therefore have decided to apply this technique to my control line model to resolve the instability problem during loop maneuver.

2.5 Basic theory of the leading edge tubercles

2.5.1 Introduction to humpback whale and leading edge tubercles

The humpback whale (Megaptera novaeangliae) is a species of baleen whale. It is one of the larger rorqual species, with adults ranging in length from 12–16 m and weighing around 25–30 metric tons. Fig. 2.16

Fig. 2.16 - Humpback whales in the Southern Ocean

Despite their size, they are highly maneuverable predators with several different specialized modes of capturing their prey. Prey swims very fast and is very agile. To get these fish humpback whales need to perform maneuvers such as loop, rolls, and tight turns. When prey is abundant, the whale will swim through the school from below at a typical speed of 2.6 m/s. This lunge-feeding behavior is also used with lateral or inverted approaches. The whale will sometimes swim away from its prey and quickly reverse direction with a U-turn before lunging back through the school. This “inside loop” behavior can be completed in as little as 1.5 body lengths. Flick-feeding is another behavior that requires rapid, tight turning capability. The whale begins a dive with its flukes clear of the water flicks its tail as it submerges, and lunges to the surface with its mouth open to the resulting food-filled wave. All these maneuvers require high agility and without the essential agility they may face severe problem with their feeding. Thus, these remote humpback whales evolved in order to meet the need for it to hunt. [7]

The humpback has a distinctive body shape, with long pectoral fins and a knobby head. As a matter of fact, the humpback has the largest pectoral flippers of any whale; it is about 31% of its total body length. It has high aspect ratio and is in backswept elliptical shape, both of these features provide an efficient lifting surface. Past

research suggested that the tubercles on its flippers are functional in the way of improving maneuverability; it works like a vortex generator to help delay stall and lift stall angle. [8]

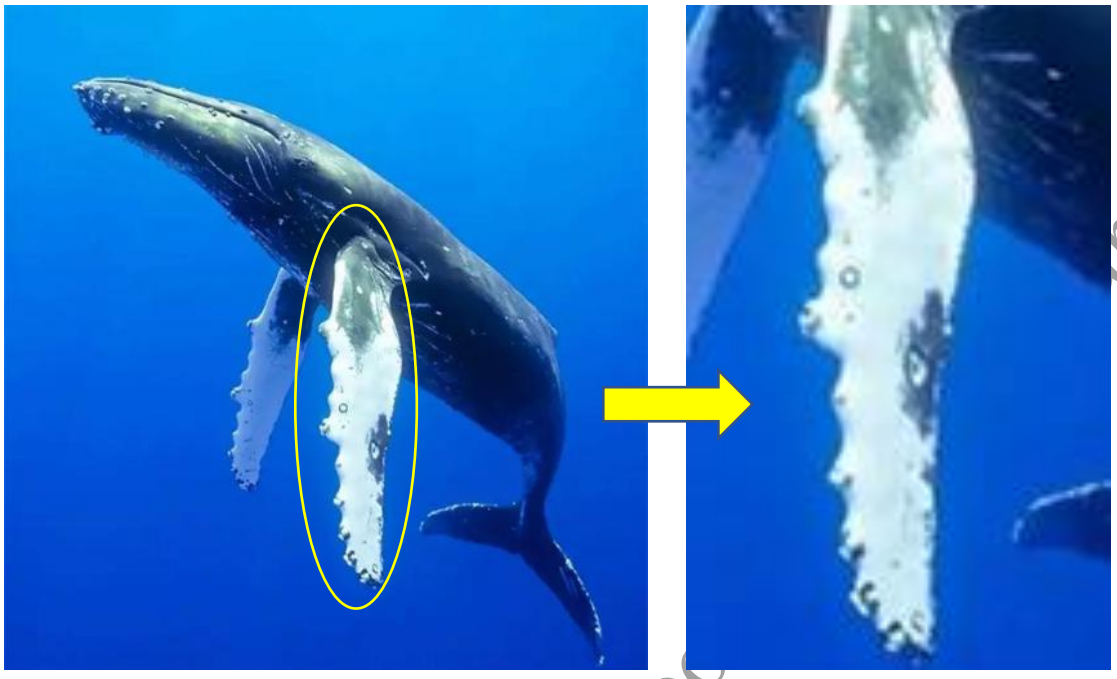

Fig. 2.17 Pectoral flipper of a humpback whale

Inspired by the flipper tubercles of humpback whales, in the following sections, I have modeled the shape of the tubercles into sinusoidal leading edge and tried to get the underlying physical mechanisms when it is applied on the wings of the control-line air model planes.

2.5.2 How leading edge tubercles work

Based on the previous studies with leading edge tubercles, the protuberances generate vortexes [Johari et al. 2007] which help maintain the lift and prevent stall in high angle of attack [Wu et al. 1991; Miklosovic et al. 2004; Fish and Lauder 2006]. The leading edge tubercles generate vortices and those vortices further establish downwash to keep the flow attach to the wing surface. Because of the existence of the downwash, the effective angle of attack α^e becomes smaller than the actual angle of attack α. Therefore, the lift force exerted on the wing is also reduced. Based on the analysis, the lift force exerted on the normal trapezoid wing will be bigger than the wing with leading edge tubercles. However, at the trapezoid wing's stall angle of attack, the downwash produced by the leading edge tubercles help keep the flow attach to the wing and reduce the flow separation. Thus, the leading edge tubercle is functioning to delay the stall of the wing although having a cost of the partially reduced lift force. This can be expressed in the below formula.

$$\alpha^e = \alpha - \frac{w}{V_0} \tag{34}$$

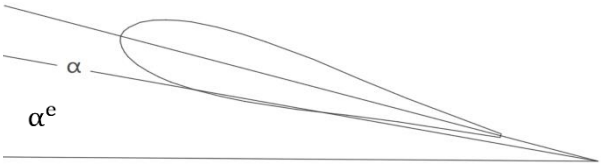

Fig. 2.18 Downwash reduces effective AoA

Where *w* is the downwash and V_0 is the velocity of the airflow. It is suggested from the above formula that the more the vortices established by the protuberances, the more delay will happen to the stall, but the more erosion to the lift will also occur.

2.5.3 Modeling leading edge tubercles for control line air model plane

Consider the shape of leading edge tubercles are most similar to sinusoid, the mathematical sinusoidal model is then employed. There are two types of sinusoidal leading edge: those with fixed amplitude and wavelength are called *fixed* sinusoidal leading edge, and those with changing amplitude and wavelength are called *distributed* sinusoidal leading edge. [9] To be relevant with the control line air model plane, this research focuses on studying the distributed leading edge, where the cord length is changing along the span of the wing.

To understand the effectiveness of the leading edge tubercles, I used the traditional trapezoid wing and a standard airfoil NACA0021, which match the model that I fly. To show how the aerodynamic properties of the wing are modified when leading edge tubercles are added, the model considers a wing which chord varies on a length scale large compared with its thickness. By having this premise, it can analytically capture the unseparated flow around the wing up to the attack angles where separation occurs. Based on the lifting-line theory, for the plane with high aspect ratio flying in a relatively small angle of attack, its change in span-wise flow and speed is much smaller than in other two directions. Therefore, we can consider in each cross section the flow is in two dimensions, and in span-wise the effect of the vortexes is different from each other.

Started from the typical sine function:

$$y = Asin(Bx) \tag{35}$$

Where A determines how “wavy” the leading edge is, and B determines how long in length each “wave” is. Put into the design context of the wing, I have related A and B with the cord length of the wing. In other words, the A and B are specified by a pair of given coefficients relevant to the cord length at each particular span-wise position.

In the typical trapezoid wing, the cord length C at a given position *x* can be calculated with the following:

$$C(x) = Cr - tan\theta * x \tag{36}$$

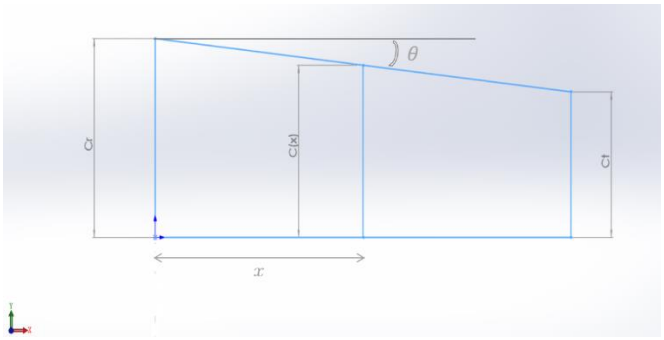

Fig. 2.19 – Trapezoid wing

In Fig. 2.19, *Cr* is the root cord length of the wing and *Ct* is the tip cord length. The back sweep angle is θ degrees.

The measurements of my model plane are: *Cr*=280mm, *Ct*=205mm, half wing span=700mm.

The amplitude of the wave at *x* position is:

$$A(x) = Ac * C(x) \tag{37}$$

And the wavelength at *x* position is:

$$\lambda(x) = \lambda c * C(x) \tag{38}$$

Where λc and Ac are a pair of given coefficients. In the past researches, Ac usually is 10% to 50% of the cord length, and λc is usually 2.5% to 10% of the cord length[13,14,15].

To convert $\lambda(x)$ into radian measure, we have:

$$B = \frac{2\pi}{\lambda(x)} \tag{39}$$

Thus, the full expression become

$$y = A(x) * sin(\frac{2\pi}{\lambda(x)} * x) + 280 \tag{40}$$

We will then be able to draw the sinusoidal leading edge as below Fig. 2.20 (the blue line). This assumed that Ac=50%*Cr and λc=5%*Cr. 280 is the root cord length.

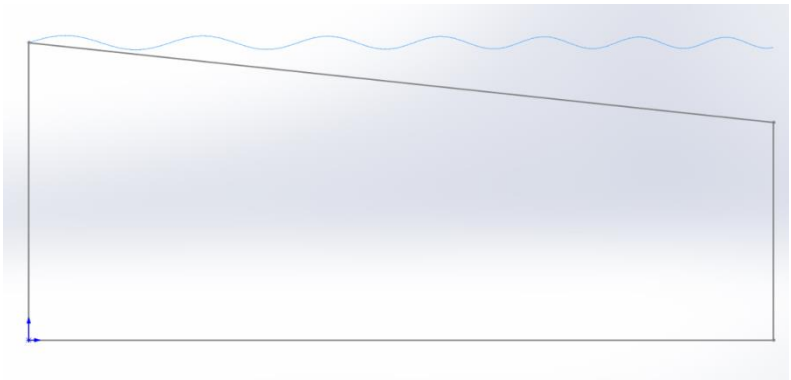

Fig. 2.20

For a trapezoid wing, there is an angle of θ degree's back sweep. Therefore, we need to do a conversion to equation (40) to be able to give the sinusoidal leading edge with the same back sweep, by adding the y-axis offset. The final equation after conversion is below:

$$y = A(x) * \sin\left(\frac{2\pi}{\lambda(x)} * x\right) - x * \tan\theta + 280 \qquad (41)$$

This (41) gives the final sinusoidal leading edge plot as illustrated below in Fig. 2.21:

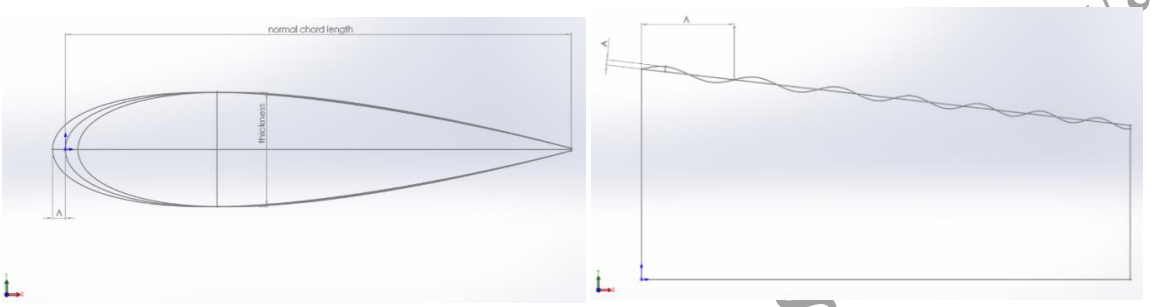

Fig. 2.21

2.5.4 3D modeling in Solid Works

Once we know how to establish the sinusoidal leading edge using equation (41), we can easily establish the 3D wing model in Solid Works using the "loft" tool and use the sinusoidal line as the guiding curve to loft. In my model plane, the standard NACA0021 airfoil is used. A sample 3D drawing is illustrated to the right in Fig. 2.22. It shows a half wing with distributed sinusoidal leading edge, with amplitude at 0.05c and the wavelength at 0.5c, where c is the root chord length of the wing.

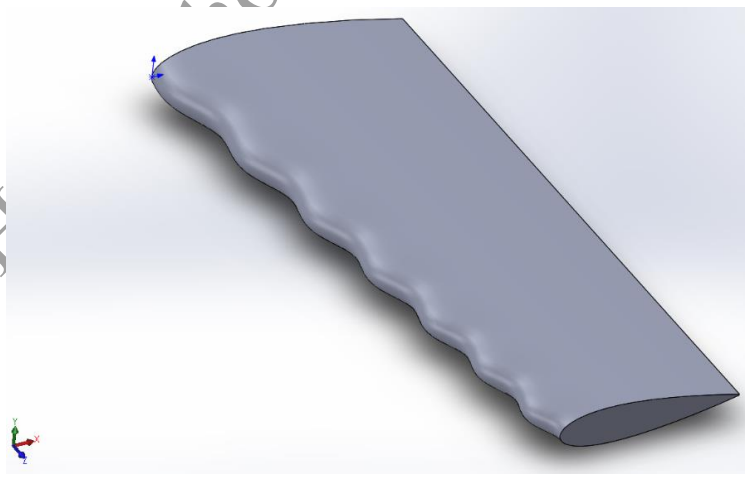

Fig. 2.22 – wing with sinusoidal leading edge

3. CFD Simulation

3.1 Introduction

In this section, Fluent, which is Computational Fluid Dynamics (CFD) software, is used to simulate the effectiveness of sinusoidal leading edge and testify how the leading edge tubercles can impact on lift, drag and angle of attack.

3.2 Meshing with ICEM

Meshing is a vital part in the simulation of CFD. It divided a complex geometry into simple elements, which discretize into local approximations of a large domain. The result of meshing impacts the simulation speed, the accuracy of the outcome and whether the outcome will converge. There are a number of different types of meshing to make adaptations to geometry.

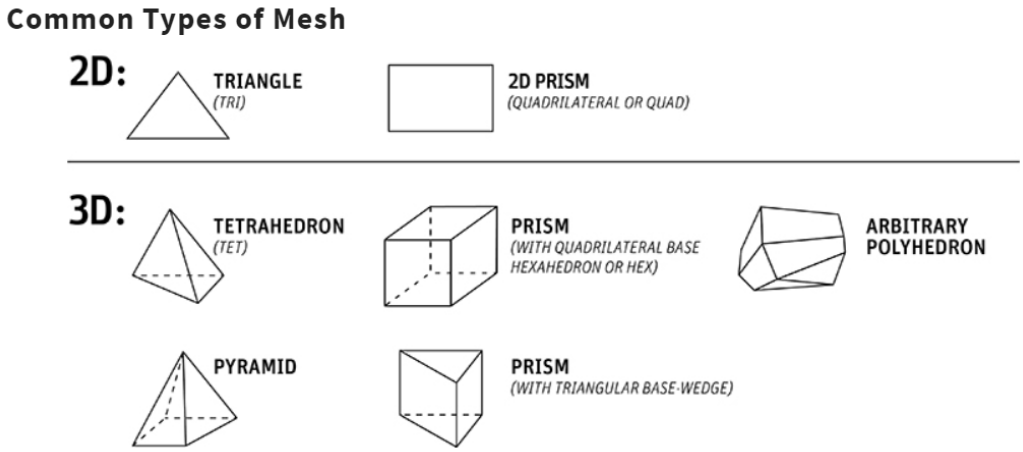

Fig. 3.1 Common types of meshing
(https://www.ansys.com/products/platform/ansys-meshing)

All these types can be divided in to two different parts: structured and unstructured grid (mesh). Typically, a structured mesh is comprised of hexahedron elements that follow a uniform pattern. An unstructured mesh does not follow a uniform pattern, usually comprised of tetrahedron elements. The structured mesh usually forms high quality meshing while the process to mesh is more difficult than unstructured mesh. The unstructured mesh on the other hand is more flexible and can be easily formed but the accuracy of the simulation may not be as good as the structured mesh. In this research, the structured mesh is used for quality and accuracy consideration.

Table 3.1 listed the 5 mesh grids that were created with different amplitude/wave lengths.

1.	2	3	4	5
0.1/0.5c	0.05/0.5c	0.025/0.5c	0.025/0.3c	0.025/0.1c
6millon grids	2million grids	2million grids	2million grids	8million grids

The Fig. 3.2 illustrates the meshing established with 0.1/0.5c sinusoidal leading edge.

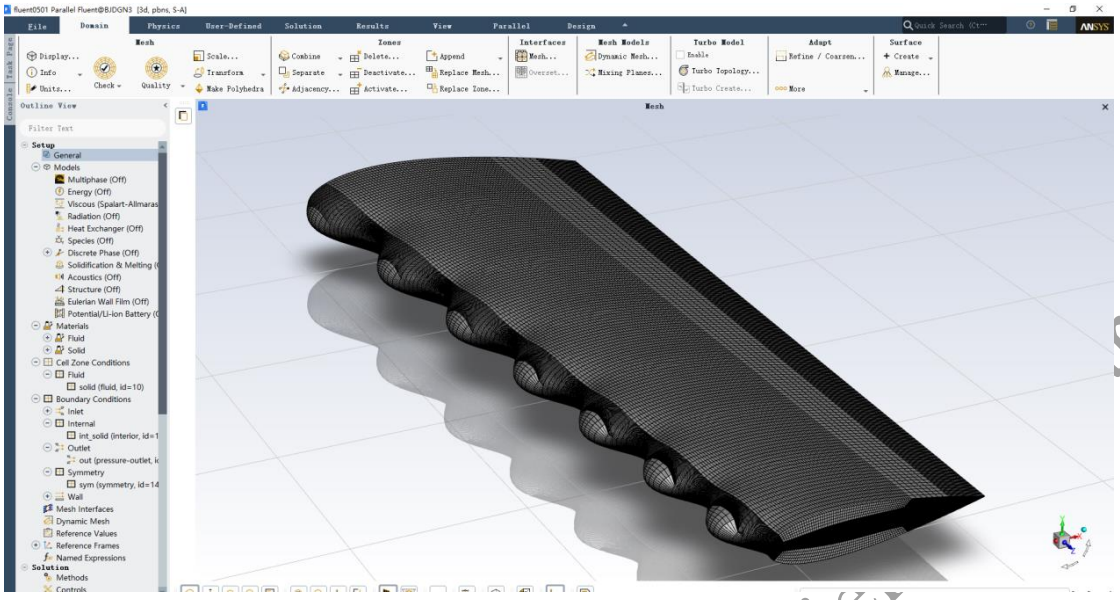

Fig. 3.2 Meshing of 0.1/0.5c leading edge wing

The flow domain, also known as enclosure, had a shape shown in the figure 3.1 below. Its length is set at 14m(50c), 4.48m (16c) in width and 8.4 (30c) in height. The root of the wing is attached to the surface of the wall. by attaching the root to the wall it can simulate a symmetric plane as only a half wing is used, Also, this allows more spaces for the wake flow. The wing is placed 5.6m (20c) to the front and 8.4m(30c) to the back. The flow domain is established as shown below and the domains are divided in structured mesh.

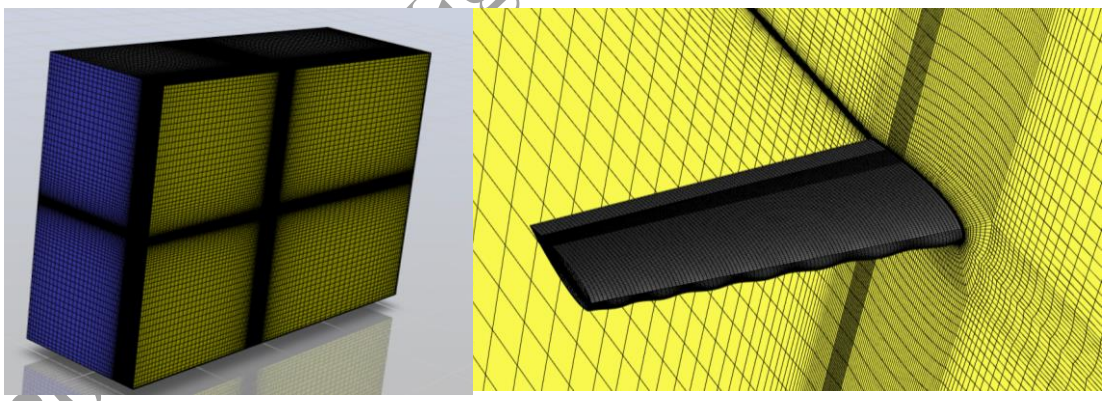

Fig. 3.3 (a) is the mesh of the flow region that will be simulated (b) is the mesh around the wing and the mesh of the wing

3.3 CFD simulation setup

3.3.1 Solver

Two types of solver can be used for the simulation in ANSYS Fluent: the pressure-based-solver and density-based-solver. The pressure-based solver is used for incompressible flow and low velocity while the density based solver is designed for high-speed compressible flow. In this simulation the pressure-based solver is chosen

to match with the control line model plane. It uses an algorism based on a general method called the projection method. The projection method is a very efficient way to do numerical solving in time-depending incompressible fluid-flow problems. It is very efficient to solve the Navier-Stokes (NS) equations. The NS-equations is an extension of the Euler equations which included the effect of viscosity. These are the fundamental equations of all the CFD algorithms and theories. NS equations contain five differential equations which include the momentum in each axis, a continuity equation and an energy equation. [10]

Continuity: $$\frac{\partial \rho}{\partial t} + \frac{\partial(\rho u)}{\partial x} + \frac{\partial(\rho v)}{\partial y} + \frac{\partial(\rho w)}{\partial z} = 0 \quad (42)$$

x-Momentum: $$\frac{\partial(\rho u)}{\partial t} + \frac{\partial(\rho u^2)}{\partial x} + \frac{\partial(\rho uv)}{\partial y} + \frac{\partial(\rho uw)}{\partial z} = -\frac{\partial p}{\partial x} + \frac{1}{Re_r}\left[\frac{\partial \tau_{xx}}{\partial x} + \frac{\partial \tau_{xy}}{\partial y} + \frac{\partial \tau_{xz}}{\partial z}\right] \quad (43)$$

y-Momentum: $$\frac{\partial(\rho v)}{\partial t} + \frac{\partial(\rho uv)}{\partial x} + \frac{\partial(\rho v^2)}{\partial y} + \frac{\partial(\rho vw)}{\partial z} = -\frac{\partial p}{\partial y} + \frac{1}{Re_r}\left[\frac{\partial \tau_{xy}}{\partial x} + \frac{\partial \tau_{yy}}{\partial y} + \frac{\partial \tau_{yz}}{\partial z}\right] \quad (44)$$

z-Momentum: $$\frac{\partial(\rho w)}{\partial t} + \frac{\partial(\rho uw)}{\partial x} + \frac{\partial(\rho vw)}{\partial y} + \frac{\partial(\rho w^2)}{\partial z} = -\frac{\partial p}{\partial z} + \frac{1}{Re_r}\left[\frac{\partial \tau_{xz}}{\partial x} + \frac{\partial \tau_{yz}}{\partial y} + \frac{\partial \tau_{zz}}{\partial z}\right] \quad (45)$$

Energy: $$\frac{\partial(E_T)}{\partial t} + \frac{\partial(vE_T)}{\partial x} + \frac{\partial(uE_T)}{\partial y} + \frac{\partial(wE_T)}{\partial z} = -\frac{\partial(\rho u)}{\partial x} - \frac{\partial(\rho v)}{\partial y} - \frac{\partial(\rho w)}{\partial z} - \frac{1}{Re_r Pr_r}\left[\frac{\partial \tau_x}{\partial x} + \frac{\partial \tau_y}{\partial y} + \frac{\partial \tau_z}{\partial z}\right] + \frac{1}{Re_r}\left[\frac{\partial}{\partial x}\left(u\tau_{xy} + v\tau_{xy} + w\tau_{xz}\right) + \frac{\partial}{\partial y}\left(u\tau_{xy} + v\tau_{yy} + w\tau_{yz}\right) + \frac{\partial}{\partial z}\left(u\tau_{xz} + v\tau_{yz} + w\tau_{zz}\right)\right] \quad (46)$$

Though the functions listed above theoretically can be solved by using calculus, it is too difficult to solve analytically. The pressure based solver helps to get solve using certain simplification and approximation. This algorism is described by considering the steady-state continuity and momentum equations in integral form shown below

$$\oint \rho \vec{v} d\vec{A} = 0 \quad (47)$$

$$\oint \rho \vec{v}\vec{v} d\vec{A} = \oint pI d\vec{A} + \oint \bar{\bar{\tau}} d\vec{A} + \int_V \vec{F} dV \quad (48)$$

3.3.2 Turbulence modelling

The approach used for turbulence modeling is the Spalart-Allmaras (SA) model. The SA model is a one-equation model; it solves a modelled transport equation for the kinematic eddy turbulence viscosity. The benefit of the SA model, compared with the double-equation, is that the calculation amount is relatively small and more stable.[11]

The model is given by the following equation:

$$\frac{\partial \tilde{v}}{\partial t} + u_j \frac{\partial \tilde{v}}{\partial x_j} = c_{b1}(1 - f_{t2})\tilde{S}\tilde{v} - \left[c_{w1} f_w - \frac{c_{b1}}{k^2} f_{t2}\right]\left(\frac{\tilde{v}}{d}\right)^2 + \frac{1}{\delta}\left[\frac{\partial}{\partial x_j}\left((v + \tilde{v})\frac{\partial \tilde{v}}{\partial x_j}\right) + c_{b2}\frac{\partial \tilde{v}}{\partial x_i}\frac{\partial \tilde{v}}{\partial x_i}\right] \quad (49)$$

And the turbulent eddy viscosity is computed from:

$$\mu_t = \rho\tilde{v} f_{v1} \tag{50}$$

Where

$$f_{v1} = \frac{X^3}{X^3 + c_{v1}^3} \tag{51}$$

$$X = \frac{\tilde{v}}{v} \tag{52}$$

Here, ρ is the density, $v = \frac{\mu}{\rho}$ is the molecular kinematic viscosity, and μ is the molecular dynamic viscosity. Here are some additional definitions:

$$\tilde{S} = \Omega + \frac{\tilde{v}}{k^2 d^2} f_{v2} \tag{53}$$

where $\Omega = \sqrt{2W_{ij}W_{ij}}$ is the magnitude of the vorticity, d is the distance from the field point to the nearest wall, and

$$f_{v2} = 1 - \frac{X}{1 + X f_{v1}} \qquad f_w = g\left[\frac{1 + c_{w3}^6}{g^6 + c_{w3}^6}\right]^{\frac{1}{6}} \tag{54}$$

$$g = r + c_{w2}(r^6 - r) \qquad r = \min\left[\frac{\tilde{v}}{\tilde{S}k^2 d^2}, 10\right] \tag{55}$$

$$f_{t2} = c_{y3} \exp(-c_{t4} X^2) \qquad W_{ij} = \frac{1}{2}\left(\frac{\partial u_i}{\partial x_j} - \frac{\partial u_j}{\partial x_i}\right) \tag{56}$$

The boundary conditions are:

$$\tilde{v}_{wall} = 0 \quad \tilde{v}_{farfeild} = 3v_\infty : to : 5v_\infty \tag{57}$$

These boundary conditions on the SA turbulence field variable correspond to turbulent kinematic viscosity values of:

$$v_{t,wall} = 0 \quad v_{t,fardfeild} = 0.210438v_\infty : to : 1.294234v_\infty \tag{58}$$

The constants are

$$c_{b1} = 0.1355\,, \delta = \frac{2}{3}, c_{b2} = 0.622, k = 0.41, c_{w2} = 0.3 \tag{59}$$

$$c_{w3} = 2, c_{v1} = 7.1, c_{t3} = 1.2, c_{t4} = 0.5, c_{w1} = \frac{c_{b1}}{k_2} + \frac{1 + c_{b2}}{\delta} \tag{60}$$

3.3.3 Fluent setup

As mentioned above, the solver is pressure-based solver using SA turbulence model for the simulation. At the temperature of 25 degree Celsius, the air density is 1.184kg/m^3. The boundary condition is the following: at the front of the cube the inlet flow velocity is 25.5m/s; at the back of the cube the boundary condition is pressure outlet. The wall where the wing is attached to is meant to make the simulation symmetric. All other boundary layers are walls. The setup for the reference value helps calculate the lift coefficient and it is the same as the simulation setup: flow velocity is 25.5m/s, density 1.184kg/m^3, temperature 298.17K, length 242.5mm which is the average chord length of the wing. The scheme is using coupled because it gains a more robust and efficient single phase implement for steady-state flow. As the convergence behavior functions very well thus the courant number stays the same.

Considering the wing is stationary, in order to simulate different angle of attack, it is required to change the direction of the inlet flow in multiple angles. We need to do force analysis to match these angles of inlet airflow so that the lift force and lift coefficient can be calculated correctly.

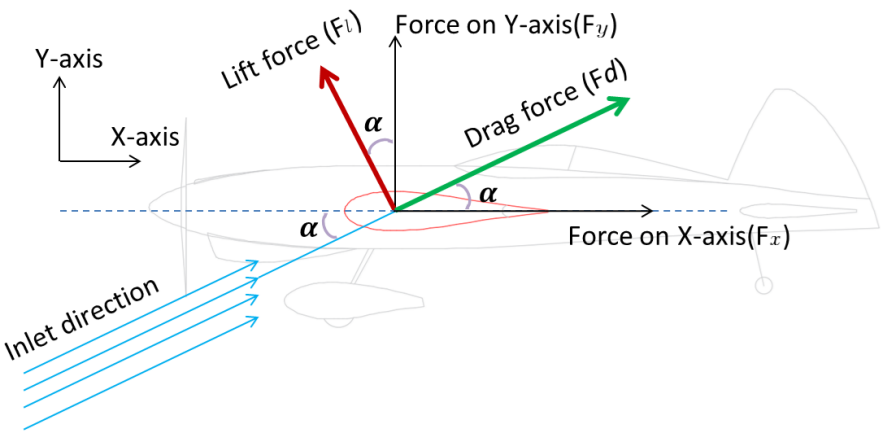

Fig. 3.4 The force analysis is relevant to the inlet direction

Assume the lift exerted on the wing is perpendicular to the inlet flow, the lift can be calculated using the following equation

$$L = Y * cos\alpha - X * sin\alpha \tag{61}$$

3.4 Simulation

The actual simulation was half successful.

The critical problem is encountered to simulate lift force. The solver takes too long (>10 hours) to produce the simulation result for a single degree. This makes it impractical to produce a coefficient curve. Usually the CFD simulation software runs on a supercomputer that is fast enough for the solver to converge. However, due to COVID-19 constraints, such a powerful computer is not accessible. In this situation, a

home computer was used to run the program, but it was way too slow to yield a valid result. As such, it made it so inefficient to make adjustments to the simulation parameters. An attempt to reduce the amount of grid was tried to see if it can produce a faster result, however, the reduced grid volume from 8 million to 2 million have impacted the validity of the simulation. The lift force returned from the solver was too small to be true (<10N). This is a follow up action to find a powerful machine to continue with the lift force simulations.

The generation of pressure distribution graph in Fluent is rather successful. The following Fig. 3.5 shows the pressure distribution on a 0.025/0.1c sinusoidal leading edge at 16 degree of inlet flow.

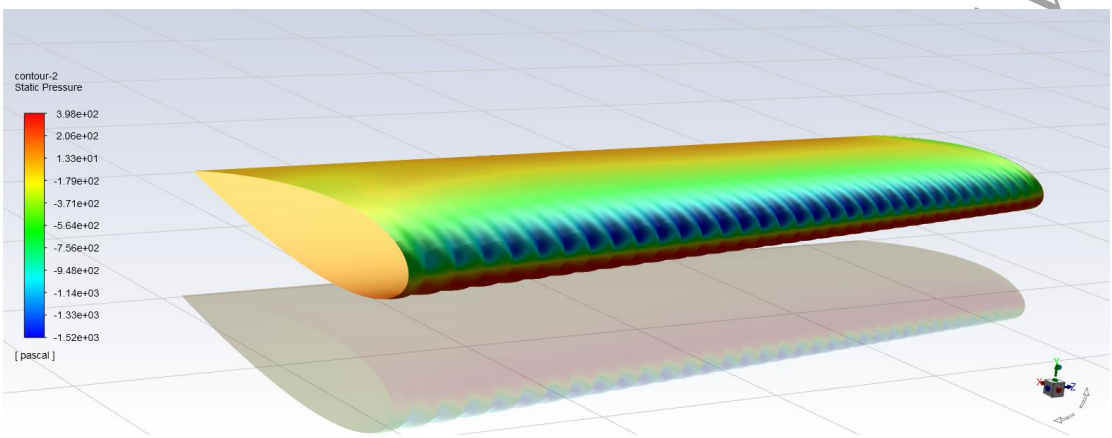

Fig. 3.5 the pressure distribution on the 0.1 0.025 sinusoidal leading edge at the wind inlet of 16°

Because of the existence of the neighboring tubercles and troughs, the airflow travels different distances from the leading edge to the trailing edge. The flow speeds therefore have more variations compare with a straight leading edge wing. This speed changes result in different pressure distributions on the wing where the pressure gradient is more adverse behind a trough than behind a tubercle. Those pressure differences have contributed to keep more vortices and airflow to attach to the wing surface at high angle of attack. This minimizes the flow separation and, consequently, delays the stall from happening. The pressure gradient and distribution patterns can be clearly seen in the simulation graph that showed in Fig. 3.5

4. Verification with actual flight

4.1 Prepare for flight data collection

In section 2.3.1, it described a way to visualize the airflow over the wing during flight. Some 60 pieces of silk threads were fixed on the wing surface of the model plane. The movements of these threads during flight are good indications of the characteristics of the air flow. It can help to identify air flow separations and capture possible stalls. A video camera is attached to the fuselage to record the flight, and the footage can be played back for examination after landing. While this experiment is easy to be carried out and intuitive, it has some obvious limitations. First, video footage cannot provide quantifiable data for analysis; second, my model has a traditional straight leading edge; it cannot be used to experiment the effectiveness of sinusoidal leading edge.

An in-flight data recorder (logger) can help to solve the first problem. The core device of an in-flight data recorder (logger) is an IMU sensor. Here, IMU stands for Inertial Measurement Unit; it is a device that measures the specific force using accelerometer, angular rate using Gyroscope and magnetic field using Magnetometers. The most commonly used IMU chips are MPU-6050 or MPU-9250. The MPU-6050 devices combine a 3-axis gyroscope and a 3-axis accelerometer on the same silicon die, together with an onboard Digital Motion Processor™ (DMP™), which processes complex 6-axis Motion Fusion algorithms. The MPU-9250 is a 9-axis Motion Tracking device that combines a 3-axis gyroscope, 3-axis accelerometer, 3-axis magnetometer and a Digital Motion Processor™ (DMP) all in a small 3x3x1mm package.

Fig. 4.1 In-flight data recorder

In this research, an integrated data recorder is used which is commercially available from www.wit-motion.com. Model WT901C with the multi-chip module MPU-9250, it is the smallest 9-axis Motion Tracking device that I can find on-line. Model plane is generally weight-sensitive and size-sensitive. The WT901 is both small in size (51.3mm*36mm*15mm) and light in weight. It weighs about 30 grams only including a built-in rechargeable battery and a CF memory card to log the flight data. Its power consumption is every low; a full charge of the internal battery can support data log for up to 5 hours. This in-flight data

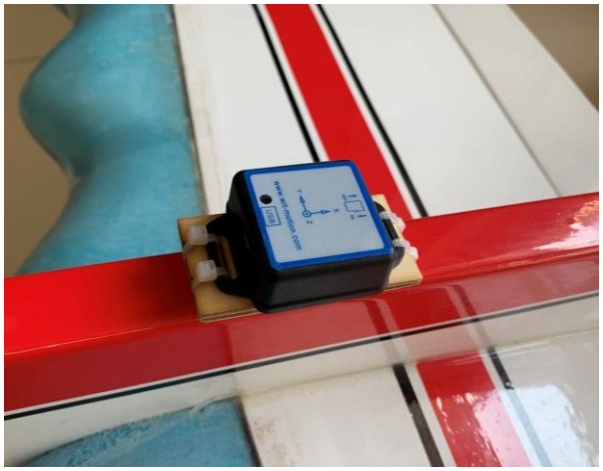

Fig. 4.2 – Install data recorder on fuselage

recorder can log angular velocity and linear acceleration in xyz axis at a data sampling speed up to 200Hz. The device is mounted on the fuselage close to the Center Gravity (CG) position so that it will not influence the model plane's aerodynamic characters. The x axis of the recorder is pointing to the tail, the y axis is pointing to the outside of the flight circle (i.e. parallel to the wing), and the z axis points to the upright direction. In such an installation position, the angular velocity of y axis can be used to analyze the movement of the plane during maneuvers. The Fig. 4.3 below is an illustration of the xyz data that logged using this device. It provides quantifiable data for analysis.

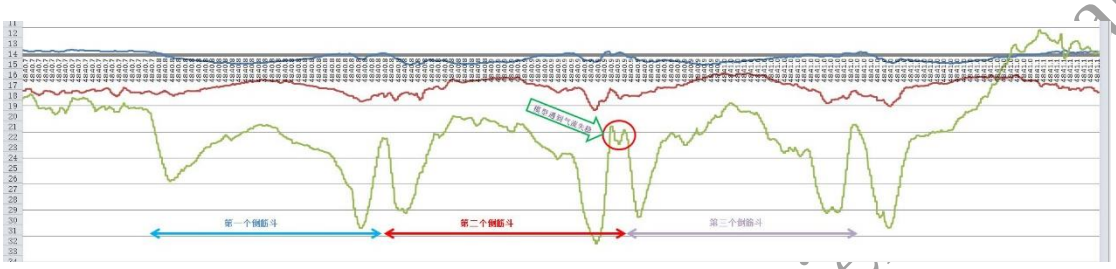

Fig. 4.3 Data sample

4.2 Flight video recording using SLR digital camera

Fig. 4.4 Video recording of flights

A Cannon EOS 650 SLR digital camera is used to record the actual flight video. The digital camera is mounted on a tripod at the height of 1.5 meters. It is positioned outside of the flying circle at the opposite position facing the maneuver. A wide-angle zoom lens (18-55mm) is used to capture the full movement. However, this camera has a limitation of fps (frame per second) for video shooting at max 50 fps speed, thus the maximum accuracy to measure time is 0.02 second. Fortunately, this accuracy is roughly ok for this research. The camera has the capability to record simultaneously video and audio. These provided a lot convenience in the analysis at the later stage.

4.3 Design and build the model plane for test flight

4.3.1 Fabrication of testing model with removable leading edge

As explained in 4.1, using my existing model plane to do test flight has an obvious limitation because all existing models do not have sinusoidal leading edge. A new model has to be designed that can satisfy the purpose to test both wing with straight leading edge and wings with a few different specs of sinusoidal leading edge. The general idea is to design a new model that has a replaceable leading edge.

Based on this thinking, the test model is designed to be identical to the existing model plane and the only difference is that the leading edge is removable. The fabrication of the test model employed the traditional building techniques. The primary material used is balsa wood. For building accuracy, the main parts of the plane were cut using a tabletop laser CNC.

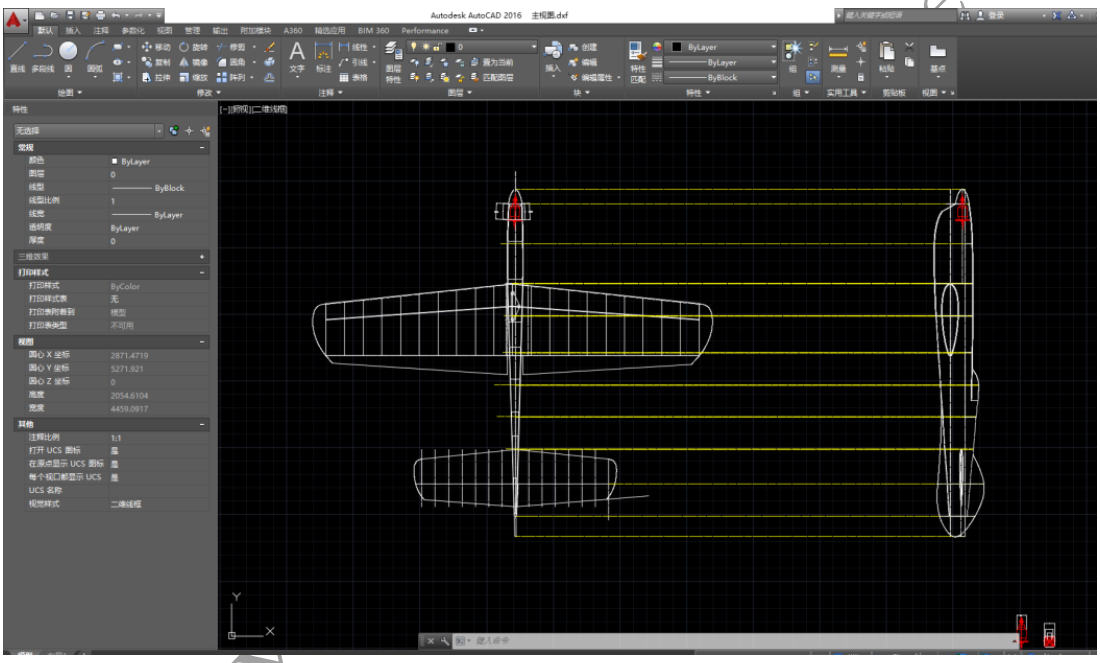

Fig. 4.5 Auto CAD plan

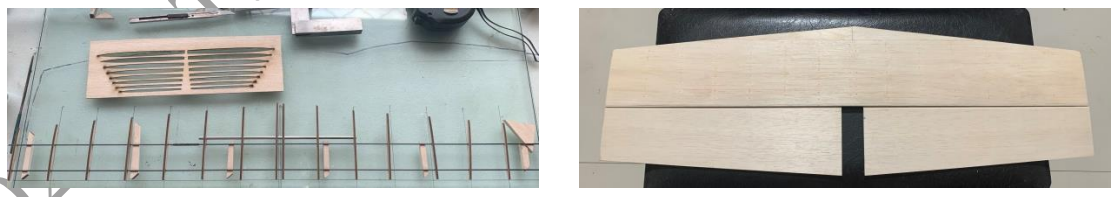

Fig. 4.6 - Stablizer and elevator

Fig. 4.7 - The model plane before final cover

Fig. 4.8 - The model plane after cover (without leading edge)

Fig. 4.9 - The model plan with the removeable leading edge

Fig. 4.10 - The removable straight leading edge

4.3.2 Fabricate sinusoidal leading edge

In addition to the traditional straight leading edge, two pairs of sinusoidal leading edge were also made. I decided to make two different types of leading-edge tubercles with different amplitudes and wavelengths. Respectively, one pair has tubercles that are 10% of the cord length, and the wavelength is 50% of the cord length. For easy reference, we call this pair 0.1/0.5c. The other pair has tubercles that are 5% of the cord length and the wavelength is 50% of the cord length. We name this group 0.05/0.5c. Why I have chosen these two sets of parameters to test? It is because, as learnt from the previous research [14], these two set of sinusoidal leading edges are supposed to have affordable impact to its lift while still have the best effectiveness to increase the critical angle of attack and delay stalls from happening.

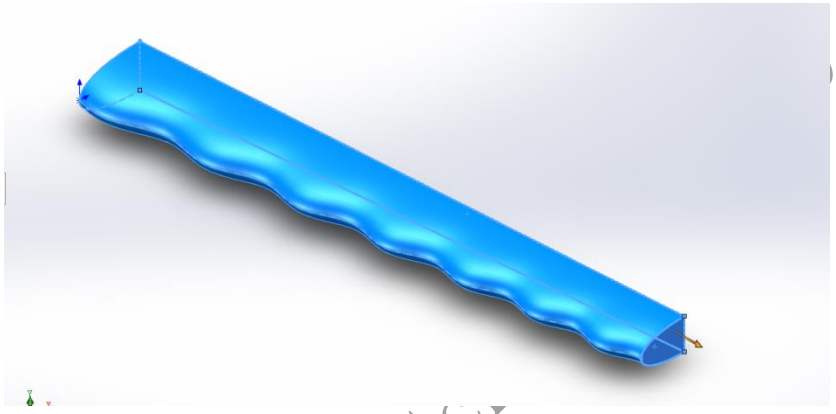

Fig. 4.11- 3D drawing of sinusoidal leading-edge in Solid Works

There are different ways to fabricate these wavy leading edges. The most accurate method is to use 3D printing. However, the materials that used for 3D printing usually are resin or nylon or acrylic, these types of material have a density around $1.35x10^3$ kg/m^3. This is much heavier than the typical building material for air model planes; for example, the density of balsa wood is only $0.09x10^3$ kg/m^3. Using 3D printing will dramatically increase the weight of the model, even if it is just to print a thin shell of the leading edge. Another challenge of 3D printing is the max allowable printing size. The length of half wing is 70 centimeters however most of the 3D printers have a maximum printing of 50 centimeters long. The availability of a large size 3D printer is an issue.

CNC machinery milling is another way to make sinusoidal leading-edge. It is both fast and accurate. However, with the impact of the COVID-19 pandemic, it is difficult to find a CNC machine that I can use to make the needed leading edge.

Having assessed the different fabrication methods, I finally chose to use the traditional air modeling building techniques to build the replaceable leading edge, that is to hand-make. The material I used is a combination of balsa wood and low density extruded polystyrene board, or XPS. XPS has a density of $0.025x10^3 kg/m^3$ which is very light; it can be easily cut into the needed shapes with a “hot wire”.

The following describes the process to make the removeable leading-edge.

Step 1. Make the sinusoidal leading-edge templates using 2mm balsa sheet. In this step, AutoCAD is used to plot the sinusoidal leading edge. And then use laser CNC cutter to make two leading-edge templates. I have a CNC laser cutter in my home, but it is a small one that can only cut up to 200mmx300mm size of objects. Therefore, I have to cut the leading-edge into 3 pieces and connect it together to the needed length. The leading-edge template is glued perpendicularly on to a base balsa board; this forms the sinusoidal leading-edge jig for the next step. As showed below.

Fig. 4.12 - sinusoidal leading-edge templates

Step 2. Cut the XPS board into long strips and glue it to the templates

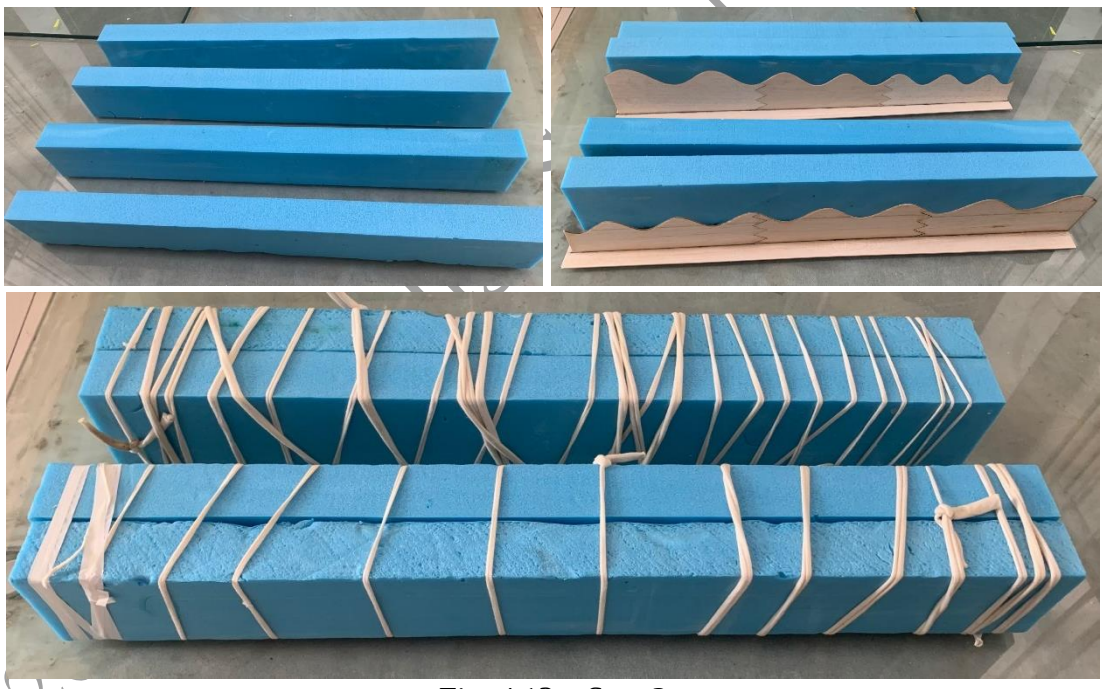

Fig. 4.13 – Step 2

Step 3. Make rough cuts using a hot wire against the balsa templates to form the basic shape.

Fig. 4.14 – rough cut to shape

Step 4. Sand it into the required shape with sandpaper and cross section templates.

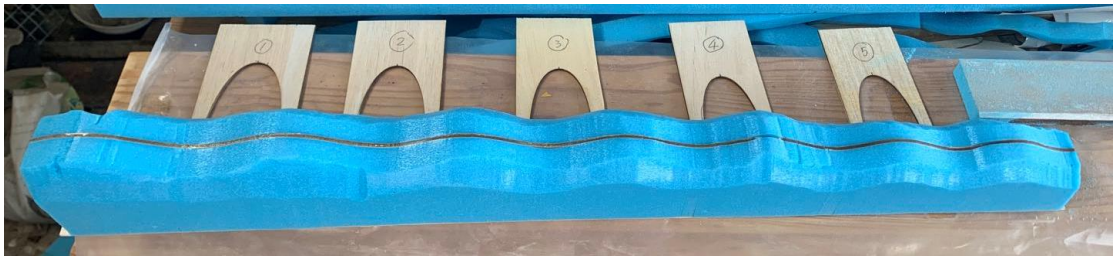

Fig. 4.15 – sanding against template

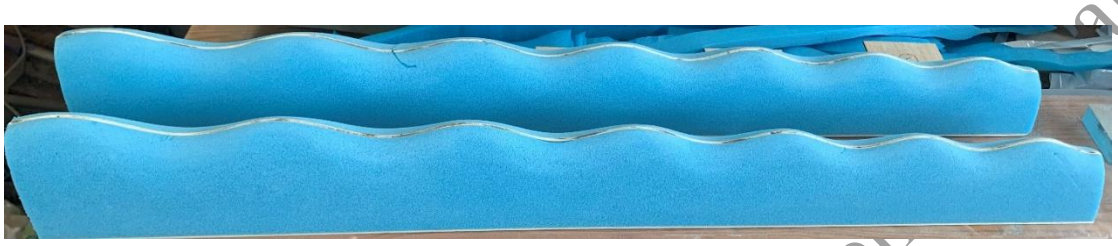

Fig. 4.16 - after sanding

Step 5. Cover the surface with fiber glass and epoxy resin to make the surface smooth and endurable. This step is necessary because the XPS material has a lot of tiny holes on the surface and is still rough after fine sanding. The surface is also very soft and could be easily damaged. Apply fiber glass and epoxy resin will solve all these problems.

Fig. 4.17 – cover with fiberglass

Step 6. Mount the leading edge to the model plane. Below picture show the two different sinusoidal leading-edge. The left is0.05/0.5c and the right is 0.1/0.5c.

Fig. 4.18 – mount to the model plane

The hand-made sinusoidal leading-edge is identical to the computer 3D design.

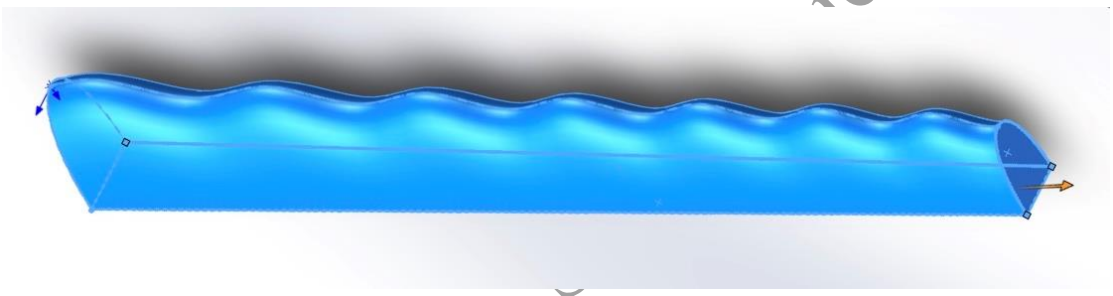

Fig. 4.19 - 3D computer drawing

4.3.3 Trimming the test model plane

Once the test model plane is built, it requires a lot of trimming before it can make perfect flights. A thorough visual inspection of all the parts and systems was conducted indoors to adjust control surface alignments, thrust line alignment, correct any distortions from the wing, elevator, fuselage, and program the on-board flight timer, etc. Once these were completed, an outdoor trimming process was conducted in the morning on August 1 2020 at the Beijing National Day School sports ground. A progressive trimming approach was used which started from short flights of 1 minutes to observe the performance and make small adjustments. The power output was adjusted to make the lap time be around 5.3". The flight time was gradually increased to 5'10" standard fighting time. The trimming process was completed after about 4 flights.

4.3.4 Flights with sinusoidal leading edge

The field testing of sinusoidal leading edge was performed 12 times during weekends between July 4 2020 and September 5 2020. More than 60 test flights were performed to collect the in-flight data. These experiments were primarily done at the Beijing National Day School sports ground. The last experiment was performed on Sep 5 at

Zhang Fang, He Bei Province, due to the air space control in the Beijing area between Sep 3 and Sep 9 for an International Fair that was held in the city.

Fig. 4.20 – 3 different type of leading-edge have been tested

The objective of these experiments was to observe and collect data of the loop maneuver. Therefore, only inside and outside loops were performed in each flight. 3 consecutive inside loops and 3 consecutive outside loops were flown repeatedly in the flight until the power cut off at 5'10". Two level laps were flown between each group of the inside/outside loops. For each test flight, 14 groups of loops could be performed, that was 21 inside loops and 21 outside loops. So, all-in-all, out of the total 60 test flights, more than 2000 inside and outside loops have been flown with the different type of leading edge. These seems to be a large quantify, however, considering the air model plane's flight performance may be influenced by the weather condition, especially by the existence of the wind at the time of flight, it is prudent to only make analysis using the data that obtained on the same day under the same weather condition. The data from different dates may only been considered as references to form the general understanding and qualitative rule of thumb.

4.4 Understanding the flight data

The in-flight data recorder logs, on a CF memory card, the x/y/z axis reading of acceleration, angular speed, and direction. Some other information is also recorded, e.g. the time stamp, temperature, etc. The sampling rate is 200Hz. In a flight of 5'10", there are total 62,000 data packets recorded for one flight. This is a big volume of data. The raw data can be imported to Excel for analysis. The following is a sample of the data.

	A	B	C	D	E	F	G	H	I	J	K	L	M	N	O	P	Q
1		ax(g)	ay(g)	az(g)	wx(deg/s)	wy(deg/s)	wz(deg/s)	AngleX(deg	AngleY(deg	AngleZ(deg	T(°)	hx	hy	hz	D0	D1	
2	08:48:13.440	0.0449	-3.1611	1.2856	0.3052	6.958	68.4204	31.1078	43.0774	168.4204	23.18	487	827	-38			
3	08:48:13.445	0.0449	-3.1611	1.2856	0.3052	6.958	68.4204	31.1298	43.0939	168.5358	23.18	484	828	-38			
4	08:48:13.450	0.0449	-3.1611	1.2856	0.3052	6.958	68.4204	31.1462	43.1158	168.6456	23.18	481	829	-38			
5	08:48:13.455	0.0415	-3.1792	1.3833	-0.4883	7.2021	68.2983	31.1682	43.1323	168.7555	23.19	479	829	-38			
6	08:48:13.460	0.0415	-3.1792	1.3833	-0.4883	7.2021	68.2983	31.1847	43.1488	168.8654	23.19	476	830	-39			
7	08:48:13.465	0.0415	-3.1792	1.3833	-0.4883	7.2021	68.2983	31.2012	43.1653	168.9697	23.19	474	830	-39			
8	08:48:13.470	0.0415	-3.1792	1.3833	-0.4883	7.2021	68.2983	31.2177	43.1818	169.0796	23.19	470	831	-39			
9	08:48:13.475	0.0366	-3.1123	1.4009	-3.2349	6.4087	67.627	31.2177	43.1927	169.184	23.2	467	831	-40			
10	08:48:13.480	0.0366	-3.1123	1.4009	-3.2349	6.4087	67.627	31.2177	43.2092	169.2828	23.2	465	831	-40			

Fig. 4.21 - in-flight data recording

4.5 Flight data analysis

The Chart tool in Excel is very helpful to visualize the recorded information and help to find out the pattern. The following two charts Fig. 4.22 and 4.23 are samples of acceleration and angular speed of the model plan in one flight.

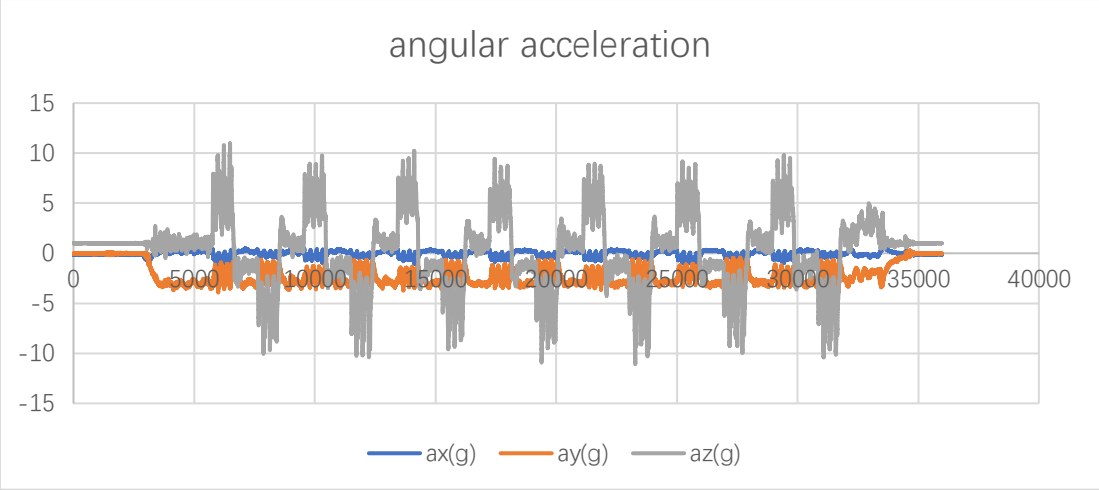

Fig. 4.22

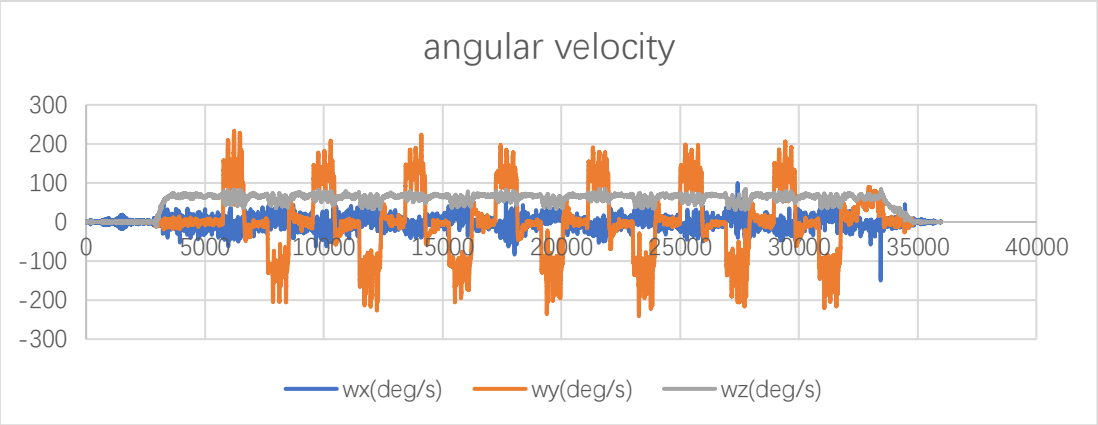

Fig. 4.23

The spikes, i.e. changes in acceleration and in angular speed, are very visible in Fig. 4.22 and Fig.4.23. These changes happen when the plane is making loop maneuvers. During the flight, when the model plane exhibits the "shake" problem, it is often coupled with sudden speed changes. Analyzing speed change can help us identify the pattern of the problem.

Fig. 4.22 is the graph of speed acceleration. It is obvious that acceleration in the z-axis is most significant. Accelerations in the other two axis are not as much as they are in the z direction. Fig. 4.23 is the graph of angular velocity. It shows that the angular velocity in y axis changed the most during the loops. The changes in x and z axis are less significant. These match very well the real flight, and therefore the data can be used for analysis.

Intensive analysis has been conducted with the y-axis angular speed. Fig. 4.24 below is an example of the isolated angular speed graph in the y-axis. It shows 7 groups of inside loops (those above 0) and 6 groups of outside loop (those below 0).

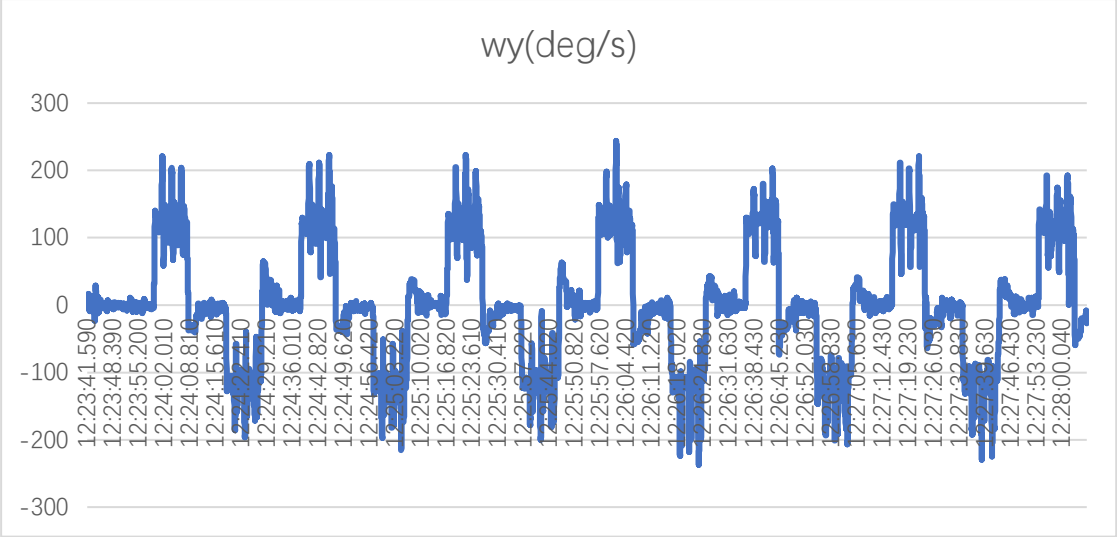

Fig. 4.24 – y-axis angular speed.

Fig. 4.25 below is the zoom-in view of one group of inside loops. Each of the "U" shape curve represents one inside loop. The angular speed changes from ~100 deg/s to ~200 deg/s in different position of the circle. This is a great match with the theoretical analysis in section 2.2.3.

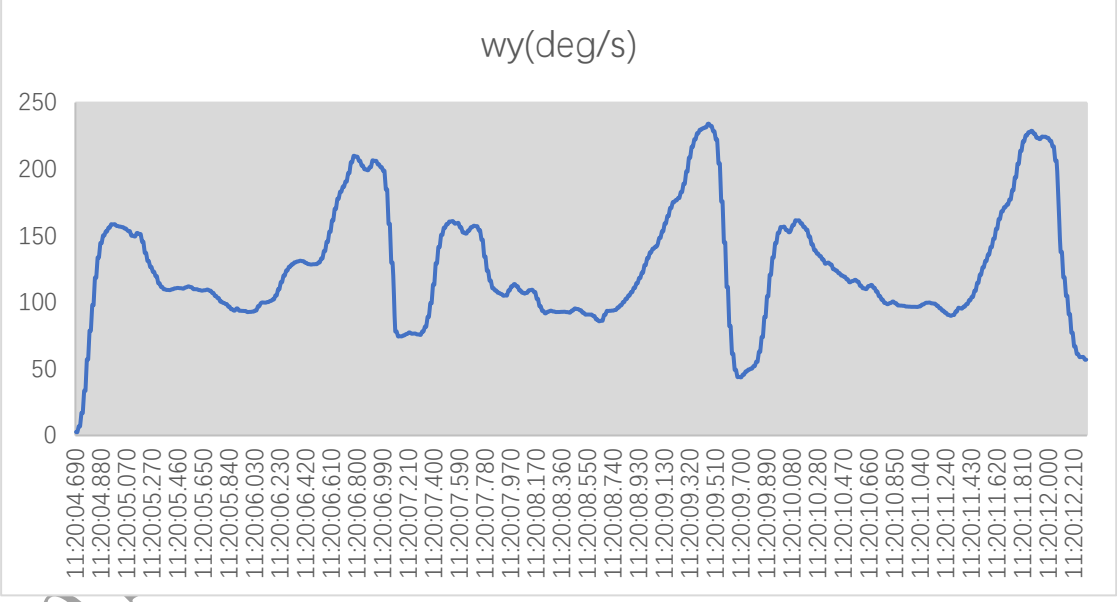

Fig. 4.25 – data of 3 consecutive inside loop

When turbulence occurs, it will show a sign of significant immediate change in the graph. By counting the number of those changes, we can determine the frequency of the occurrence in one flight. Accumulatively if we make sufficient number of loop maneuvers and count the overall occurrences, it will then have statistic meaning to compare among the difference type of leading-edges. In this research, 3 types of leading-edge were tested. By comparing the turbulence occurrences among the three leading-edges, we can understand the general effectiveness of the sinusoidal tubercles in improving the stability of the model plane.

As stated earlier, model plane's flight performance may be influenced by the weather condition, especially by the existence of the wind at the time of flight; it is prudent to make analysis using only the data that obtained on the same day under the same weather condition. The data from different dates may only been considered as references to form the general understanding and qualitative rule of thumb.

In the real flight, the environmental air condition may change even during the same flight. To minimize this influence on the analysis, we can shorten the observation window to the duration of each group of 3 loops. Experience tells me that turbulence seldom happen in the first loop, and therefore, the curve of the first loop are used as the base line reference for the consecutive two loops. When the curve of the 2nd and 3rd loop is significantly deviated from the shape of the first curve, it generally indicated an occurrence of turbulence.

Chart 4.26 illustrates how turbulence is identified in the consecutive 3 loops. This is recorded as the fourth group of inner loops in the second flight with the regular leading edge, on Sep 5 2020. The curve of the second loop had an unusual change in the middle of the slope. This immediate change of the angular velocity is identified as turbulence occurred at that moment. This is cross checked and confirmed with the simultaneous video and audio recording.

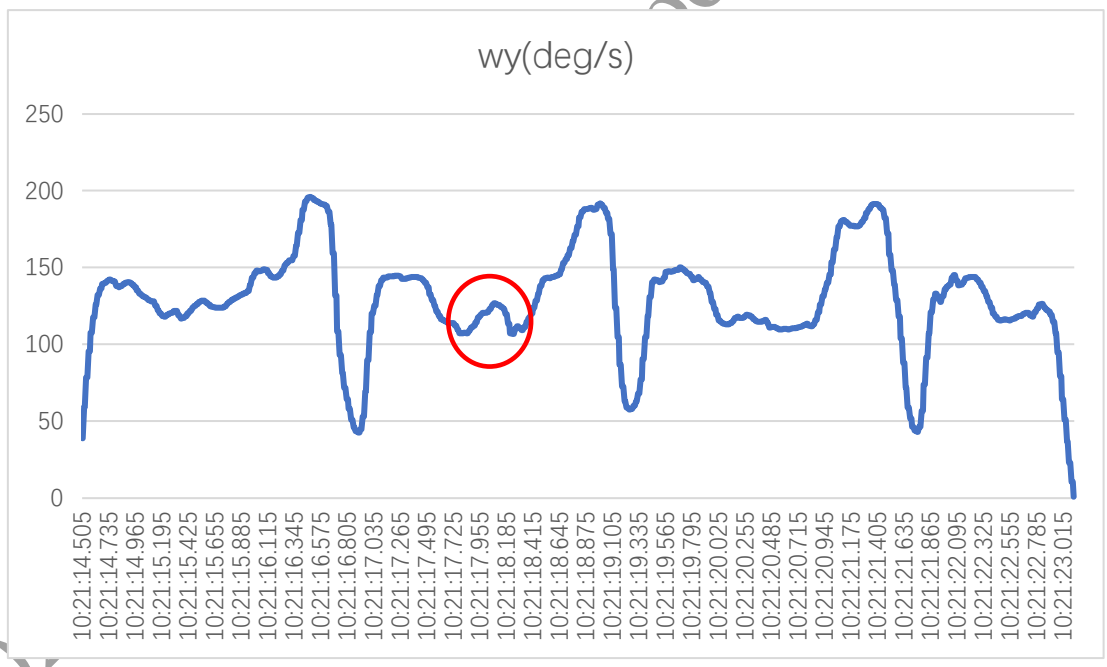

Fig. 4.26 – Identify turbulence

The 6 graphs below show the flight data that have been collected for the 3 different leading-edges. These data were collected at the same practice field, on the same day (September 5 2020), and the wind speed was steadily <2m/s. For each flight, around 40 loops were performed, so 6 flights gave total 240 loops to be examined. For each type of leading edge, two flights or 80 loops have been logged. With this amount of data, the significance of the leading edge tubercles should reveal. In addition to the data log, videos and audios were also recorded for each flight.

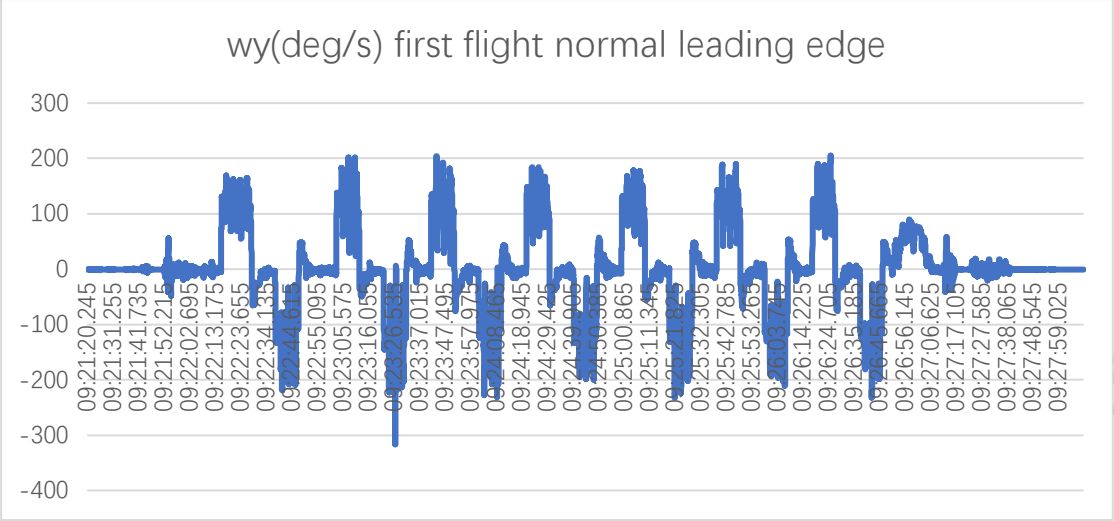

Fig 4.27 – Sep 5 first flight with regular leading edge

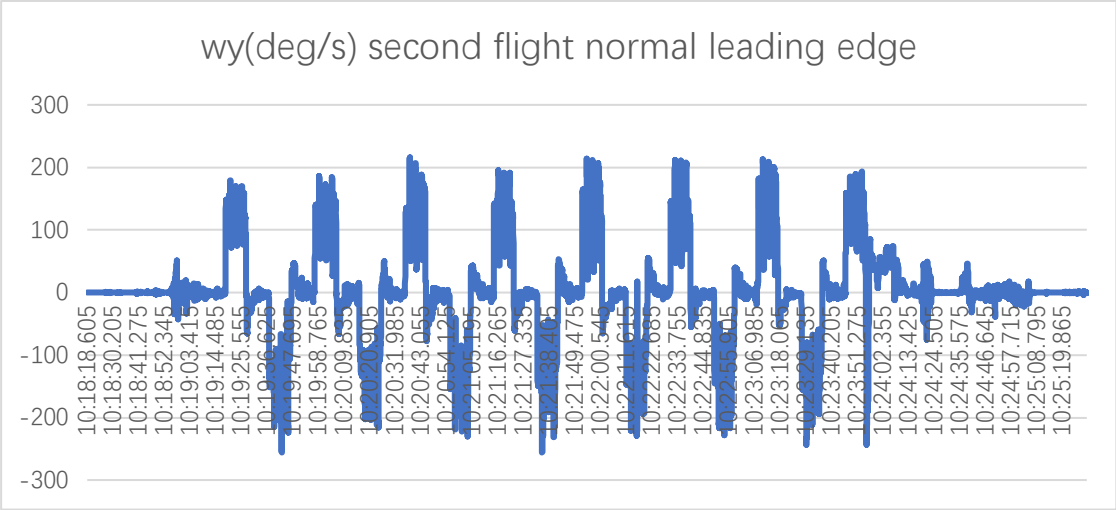

Fig 4.28 – Sep 5 second flight with regular leading edge

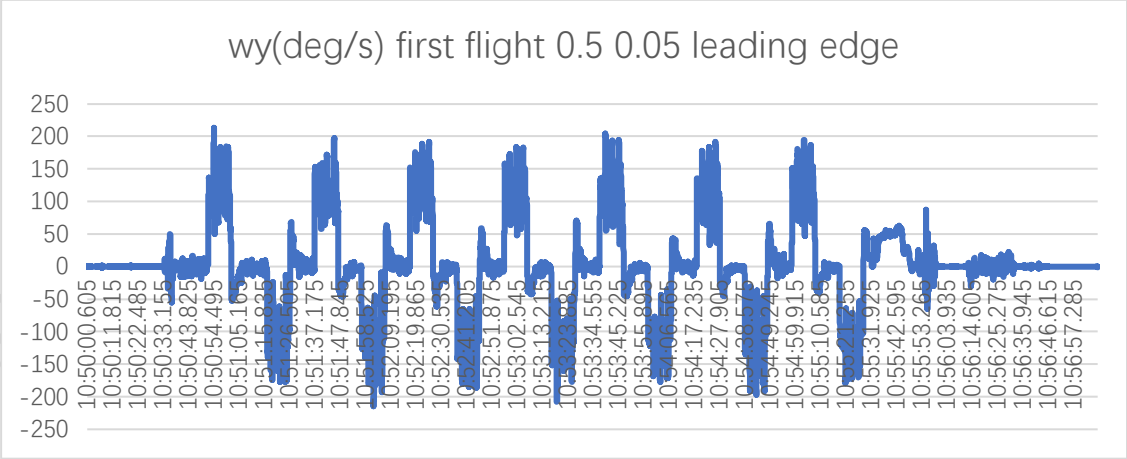

Fig 4.29 – Sep 5 first flight with 0.05/0.5c sinusoidal leading edge

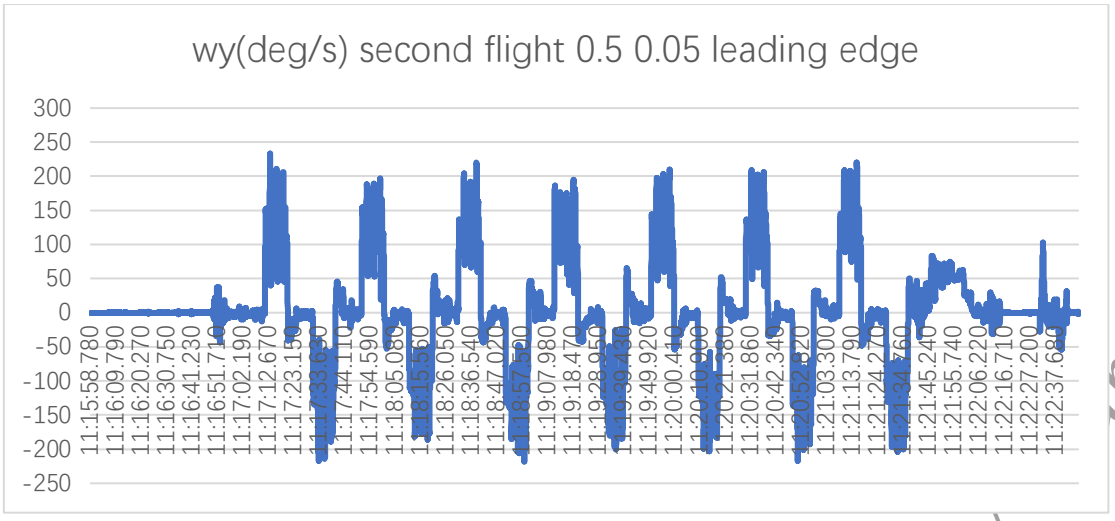

Fig 4.30 – Sep 5 second flight with 0.05/0.5c sinusoidal leading edge

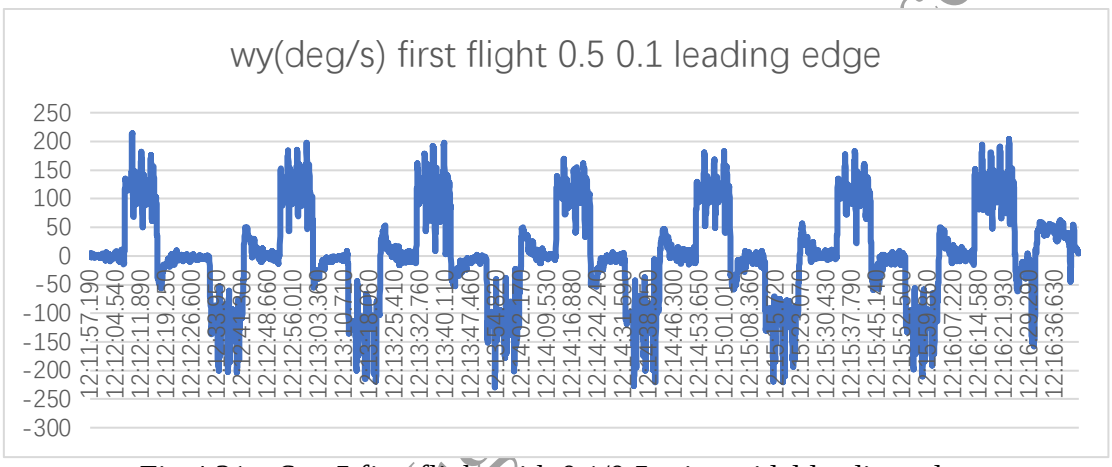

Fig 4.31 – Sep 5 first flight with 0.1/0.5c sinusoidal leading edge

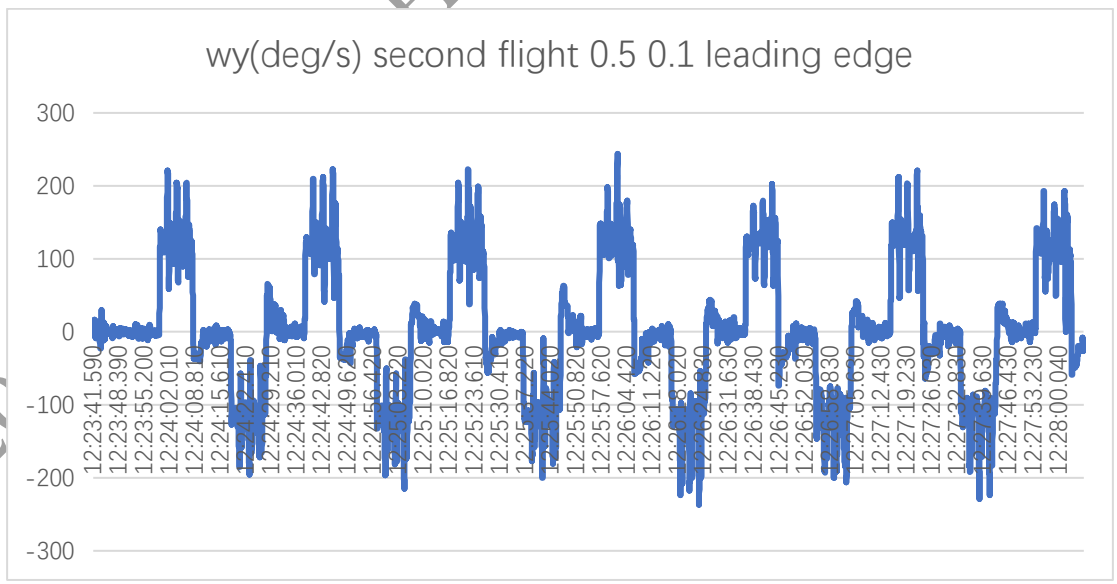

Fig 4.32 – Sep 5 second flight with 0.1/0.5c sinusoidal leading edge

Applying the same logic, the analysis was done for all the 6 flights showed above. As an outcome:

- With the normal leading edge, the sign of turbulence occurred 7 times out of 84 loops. The occurrence is 8.3%.
- With the sinusoidal leading edge of 0.05/0.5c, the sign of turbulence occurred 3 times out of 84 loops. The occurrence is 3.6%.
- With the sinusoidal leading edge of 0.1/0.5c, the sign of turbulence occurred 2 times out of 78 loops. The occurrence is 2.6%.

4.6 Conclusion of field testing

From this analysis, it is evident that, compare with the normal leading edge, the sinusoidal leading edge has significantly reduced the occurrence of turbulence by more than 56%. However, in between the two sinusoidal leading edges, the increased amplitude of the tubercles did not show meaningful statistical differences to further improve the stability of the model plane.

Another interesting observation from the test flights have showed that the battery power consumption using the sinusoidal leading edge is slightly lower than that of the regular leading edge by approximately 3% per flight. As measured after the flight, the battery reserve was 25% with the 0.05/0.5c sinusoidal leading edge, while it was 22% with the regular leading edge. This suggested another potential benefit of using sinusoidal leading edge to save energy. It is likely that leading edge tubercles may not only delay stalls, but also improve the drag coefficient of the airfoil. More tests and research will be required to prove this assumption. Although it is not the focus of this paper, it can be an interesting follow up research to be conducted afterwards.

5. Conclusion

In conclusion, F2B control line model plane has a long haunting problem in performing high-dynamic maneuvers, specifically, the model plane would sometimes lost balance and become unstable in flying consecutive loop maneuvers in no-wind or little-wind conditions. In this research, it is proved that during loop maneuvers, the wing needs to generate much larger lift to provide sufficient centripetal force for the model to accomplish the loop. This larger lift is obtained from the wing by flying in high angle of attacks (AoA). This high AoA is close to the critical angle of attack to stall. This phenomenon is further worsened by the turbulent air left from the previous loop on the same flight path, which make the 2nd and 3rd loops to exceed the critical AoA, at which moment the airflow on the wing separate, and result in sudden drop in lift. This causes the plane to stall and become unstable. In windy conditions, the wind helps to blew away the turbulent air on the flight path, and therefore, the plane is less likely to be impacted by the previous loop, and hence it is less likely for the stall problem to happen.

Flow control technique is used to improve the model plane's performance in situation of high angle of attacks by employing sinusoidal tubercles on the leading edge. With CFD simulation, it is showed that because of the existence of the neighboring tubercles and troughs, the airflow travels different distances from the leading edge to the trailing edge. The airflow speeds therefore have more variations compare with a straight edge wing. This speed changes result in different pressure distributions on the wing. The pressure differences have contributed to keep more vortices and airflow to attach to the wing surface at high angle of attack. This minimizes the flow separation and, consequently, delays or weakens the stalls to happen.

Intensive field test with actual flights have further confirmed the root cause of the problem and the general effectiveness of using sinusoidal leading edge to improve stability in control line model plane's loop maneuver. Under the same condition, the wing with tubercles has reduced more than 56% of the occurrences of turbulence. It also indicated that by purely increasing the amplitude of the tubercles does not provide meaningful improvements to further delay stalls but rather increased the complexity of the wing structure and increased difficulties of fabrication.

6. Follow up

The primary follow-up work is to find a much faster and powerful computer for CFD simulation, so that the lift coefficient curve can be established for different sinusoidal leading edges with different combination of parameters. The COVID-19 pandemic in the past several months has made it difficult to access to these machines in the labs.

Another follow up, if practically viable, is to employ wind tunnel to experiment different leading edges, as the wind tunnel provides a more ideal testing environment than the open field. With the wind tunnel, the actual lift and drag properties can be measured and studied. The challenge with this is the availability of the right size of wind tunnel that can suit the size of the model plane with the 1.5 wingspan. The cost affordability of employing a wind tunnel may also be a challenge.

Last but not least, as described in the last part of section 3, an interesting observation from the test flights has showed that the sinusoidal leading edge may have contributed to power savings in the flights. It hinted that the tubercles may not only delay stalls, but also improve drag coefficient of the airfoil. More tests and research efforts are required to confirm the finding and to explain the theories behind. Although it is not the focus of this paper, it can be an interesting follow up to be explored.

References:

[1] Aleks Udris, Vortex Generators: Preventing Stalls At High And Low Speeds (2015)

[2] Sporting Code Section 4 – F2 Control Line, FAI, 16 Dec 2019

[3] Sporting Code Section 4 – F2 Annex 4J, FAI, 16 Dec 2019

[4] The new rational manager, by Charles H. Kepner, Benjamin B. Tregoe, Princeton Research Press; Updated Edition (December 1, 1997)

[5] Yousefi, Kianoosh; Saleh, Reza "Three-dimensional suction flow control and suction jet length optimization of NACA 0012 wing" (2015-01-23)

[6] Intelligent Control and Autonomy Branch facilities "Active flow control Laboratory" (2008-2-29)

[7] Wikipedia "Humpback whale"

[8] Michael Jordan Stanway "Hydrodynamic effects of leading-edge tubercles on control surfaces and in flapping foil propulsion." (2008-2)

[9] Ernst A. van Nierop, Silas Alben, and Michael P. Brenner "How Bumps on Whale Flippers Delay Stall: An Aerodynamic Model" (2008-2-27)

[10] Glenn Research Center "Navier-Stokes Equations 3-dimensional-unsteady" (2015-5-5)

[11] Langley Research Center "Turbulence Modeling Resource" (2018-8-6)

[12] Jonathan Borg, "The effect of leading edge serrations on dynamic stall", University of Southampton Research Repository ePrints Soton, 2012

[13] 祁武超，李东伟，田素梅，"仿驼背鲸鳍机翼流动特性分析"，沈阳航空航天大学学报，Vol. 34 No. 5, Oct. 2017

[14] 潘翀，陈皇，王晋军，"可变正弦前缘对直机翼气动性能影响的研究"，实验流体力学，Vol. 27, NO. 4, Aug. 2013

[15] 田素梅，李东伟，祁武超，"大攻角下仿驼背鲸鳍叶片气动性能分析"，沈阳航空航天大学学报，Vol. 35, No. 3, Jun 2018

[16] P. Watts & F.E. Fish, "The influence of passive, leading edge tubercles on wing performance"

Appendix

A1. Overall thinking process applied in this research

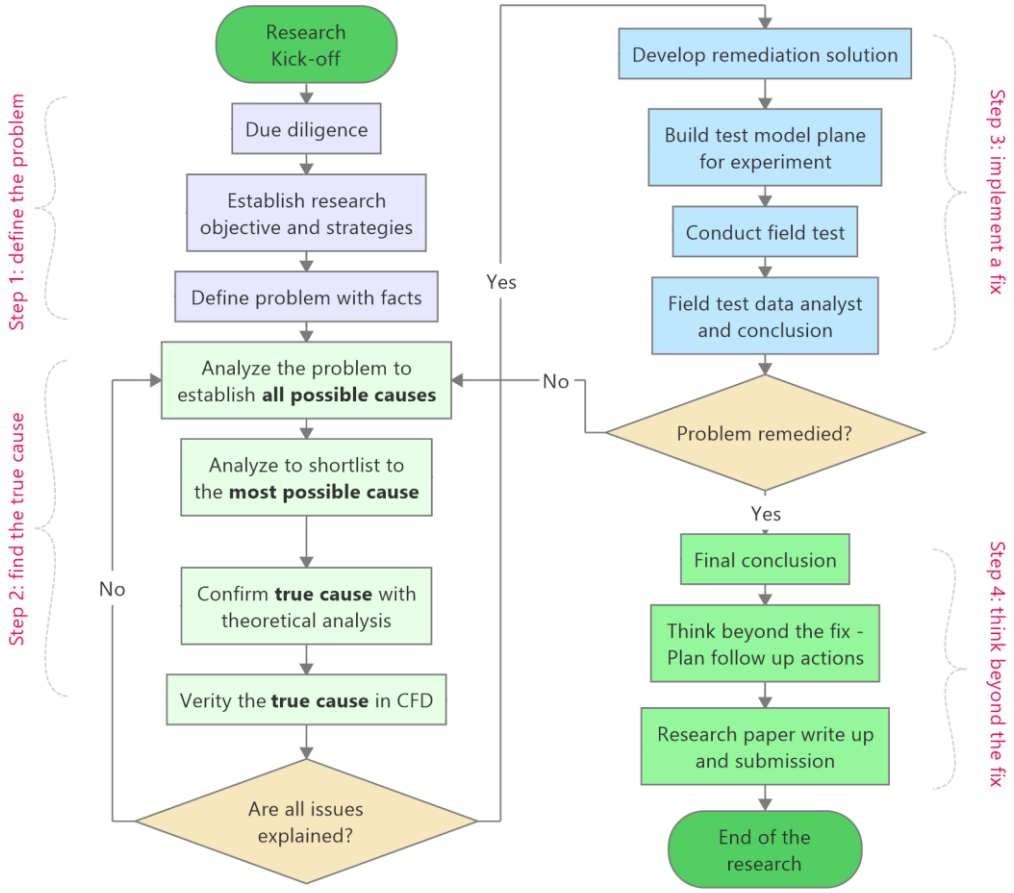

A2. Research plan/schedule

A2.1 High level research plan/schedule

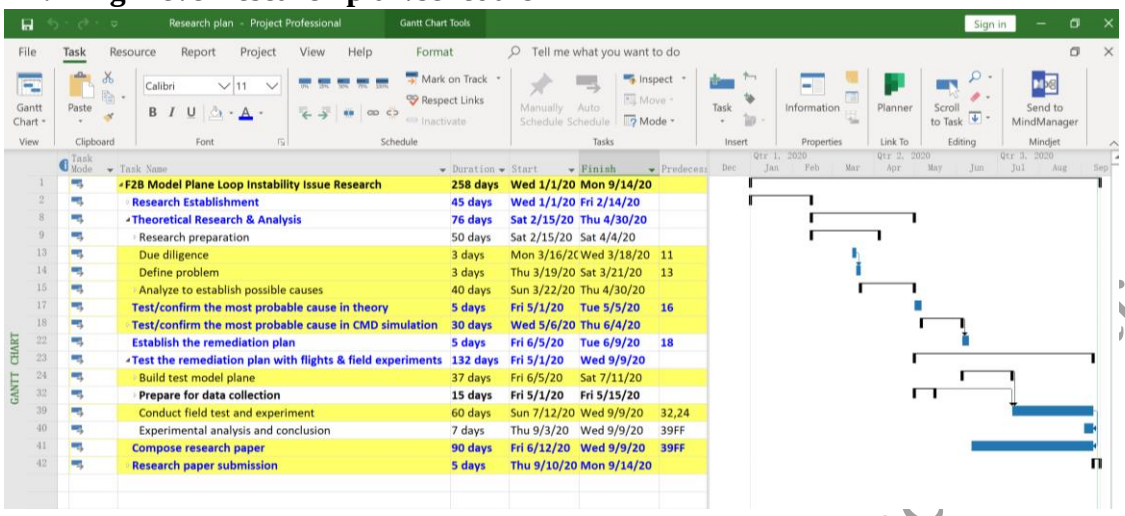

	Task Mode	Task Name	Duration	Start	Finish	Predecessors
1		**F2B Model Plane Loop Instability Issue Research**	**258 days**	**Wed 1/1/20**	**Mon 9/14/20**	
2		**Research Establishment**	**45 days**	**Wed 1/1/20**	**Fri 2/14/20**	
8		**Theoretical Research & Analysis**	**76 days**	**Sat 2/15/20**	**Thu 4/30/20**	
9		Research preparation	50 days	Sat 2/15/20	Sat 4/4/20	
13		Due diligence	3 days	Mon 3/16/20	Wed 3/18/20	11
14		Define problem	3 days	Thu 3/19/20	Sat 3/21/20	13
15		Analyze to establish possible causes	40 days	Sun 3/22/20	Thu 4/30/20	
17		**Test/confirm the most probable cause in theory**	**5 days**	**Fri 5/1/20**	**Tue 5/5/20**	**16**
18		**Test/confirm the most probable cause in CMD simulation**	**30 days**	**Wed 5/6/20**	**Thu 6/4/20**	
22		**Establish the remediation plan**	**5 days**	**Fri 6/5/20**	**Tue 6/9/20**	**18**
23		**Test the remediation plan with flights & field experiments**	**132 days**	**Fri 5/1/20**	**Wed 9/9/20**	
24		Build test model plane	37 days	Fri 6/5/20	Sat 7/11/20	
32		**Prepare for data collection**	**15 days**	**Fri 5/1/20**	**Fri 5/15/20**	
39		Conduct field test and experiment	60 days	Sun 7/12/20	Wed 9/9/20	32,24
40		Experimental analysis and conclusion	7 days	Thu 9/3/20	Wed 9/9/20	39FF
41		**Compose research paper**	**90 days**	**Fri 6/12/20**	**Wed 9/9/20**	**39FF**
42		**Research paper submission**	**5 days**	**Thu 9/10/20**	**Mon 9/14/20**	

A2.2 Detail research plan/schedule

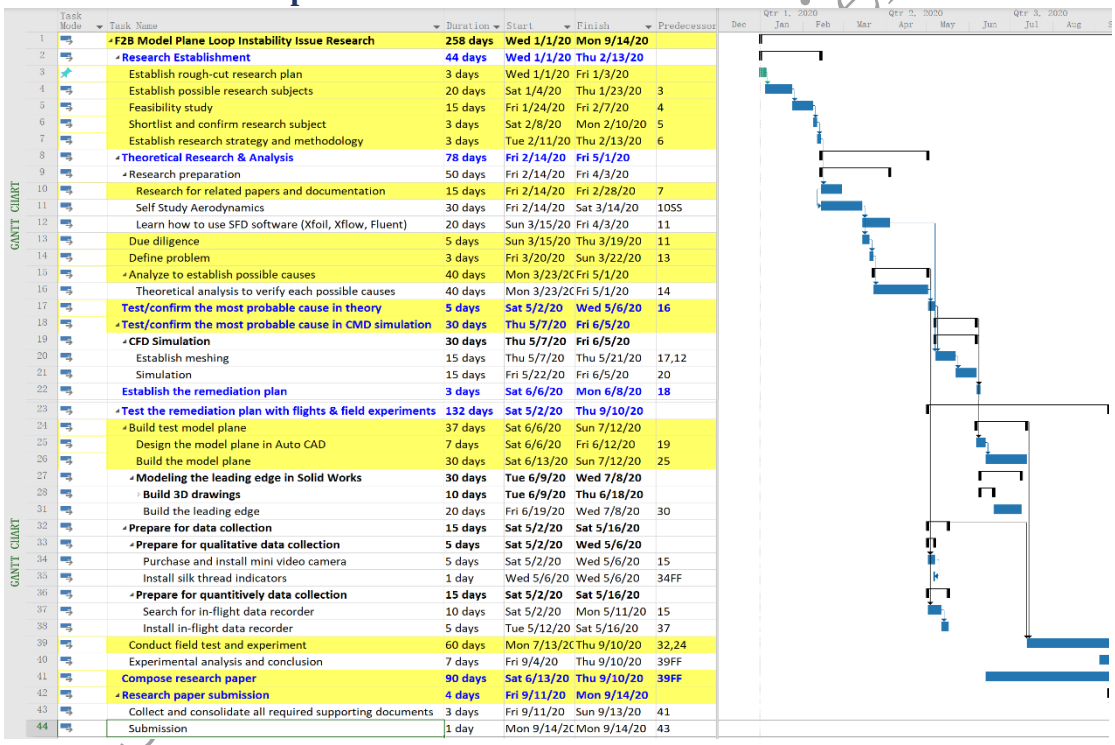

	Task Mode	Task Name	Duration	Start	Finish	Predecessors
1		**F2B Model Plane Loop Instability Issue Research**	**258 days**	**Wed 1/1/20**	**Mon 9/14/20**	
2		**Research Establishment**	**44 days**	**Wed 1/1/20**	**Thu 2/13/20**	
3		Establish rough-cut research plan	3 days	Wed 1/1/20	Fri 1/3/20	
4		Establish possible research subjects	20 days	Sat 1/4/20	Thu 1/23/20	3
5		Feasibility study	15 days	Fri 1/24/20	Fri 2/7/20	4
6		Shortlist and confirm research subject	3 days	Sat 2/8/20	Mon 2/10/20	5
7		Establish research strategy and methodology	3 days	Tue 2/11/20	Thu 2/13/20	6
8		**Theoretical Research & Analysis**	**78 days**	**Fri 2/14/20**	**Fri 5/1/20**	
9		Research preparation	50 days	Fri 2/14/20	Fri 4/3/20	
10		Research for related papers and documentation	15 days	Fri 2/14/20	Fri 2/28/20	7
11		Self Study Aerodynamics	30 days	Fri 2/14/20	Sat 3/14/20	10SS
12		Learn how to use SFD software (Xfoil, Xflow, Fluent)	20 days	Sun 3/15/20	Fri 4/3/20	11
13		Due diligence	5 days	Sun 3/15/20	Thu 3/19/20	11
14		Define problem	3 days	Fri 3/20/20	Sun 3/22/20	13
15		Analyze to establish possible causes	40 days	Mon 3/23/20	Fri 5/1/20	
16		Theoretical analysis to verify each possible causes	40 days	Mon 3/23/20	Fri 5/1/20	14
17		**Test/confirm the most probable cause in theory**	**5 days**	**Sat 5/2/20**	**Wed 5/6/20**	**16**
18		**Test/confirm the most probable cause in CMD simulation**	**30 days**	**Thu 5/7/20**	**Fri 6/5/20**	
19		**CFD Simulation**	**30 days**	**Thu 5/7/20**	**Fri 6/5/20**	
20		Establish meshing	15 days	Thu 5/7/20	Thu 5/21/20	17,12
21		Simulation	15 days	Fri 5/22/20	Fri 6/5/20	20
22		**Establish the remediation plan**	**3 days**	**Sat 6/6/20**	**Mon 6/8/20**	**18**
23		**Test the remediation plan with flights & field experiments**	**132 days**	**Sat 5/2/20**	**Thu 9/10/20**	
24		Build test model plane	37 days	Sat 6/6/20	Sun 7/12/20	
25		Design the model plane in Auto CAD	7 days	Sat 6/6/20	Fri 6/12/20	19
26		Build the model plane	30 days	Sat 6/13/20	Sun 7/12/20	25
27		**Modeling the leading edge in Solid Works**	**30 days**	**Tue 6/9/20**	**Wed 7/8/20**	
28		**Build 3D drawings**	**10 days**	**Tue 6/9/20**	**Thu 6/18/20**	
31		Build the leading edge	20 days	Fri 6/19/20	Wed 7/8/20	30
32		**Prepare for data collection**	**15 days**	**Sat 5/2/20**	**Sat 5/16/20**	
33		**Prepare for qualitative data collection**	**5 days**	**Sat 5/2/20**	**Wed 5/6/20**	
34		Purchase and install mini video camera	5 days	Sat 5/2/20	Wed 5/6/20	15
35		Install silk thread indicators	1 day	Wed 5/6/20	Wed 5/6/20	34FF
36		**Prepare for quantitively data collection**	**15 days**	**Sat 5/2/20**	**Sat 5/16/20**	
37		Search for in-flight data recorder	10 days	Sat 5/2/20	Mon 5/11/20	15
38		Install in-flight data recorder	5 days	Tue 5/12/20	Sat 5/16/20	37
39		Conduct field test and experiment	60 days	Mon 7/13/20	Thu 9/10/20	32,24
40		Experimental analysis and conclusion	7 days	Fri 9/4/20	Thu 9/10/20	39FF
41		**Compose research paper**	**90 days**	**Sat 6/13/20**	**Thu 9/10/20**	**39FF**
42		**Research paper submission**	**4 days**	**Fri 9/11/20**	**Mon 9/14/20**	
43		Collect and consolidate all required supporting documents	3 days	Fri 9/11/20	Sun 9/13/20	41
44		Submission	1 day	Mon 9/14/20	Mon 9/14/20	43